# High-entropy alloys

*Easo P. George* [1,2]*, *Dierk Raabe[3] and Robert O. Ritchie* [4,5]

Abstract | Alloying has long been used to confer desirable properties to materials. Typically, it involves the addition of relatively small amounts of secondary elements to a primary element. For the past decade and a half, however, a new alloying strategy that involves the combination of multiple principal elements in high concentrations to create new materials called high-entropy alloys has been in vogue. The multi-dimensional compositional space that can be tackled with this approach is practically limitless, and only tiny regions have been investigated so far. Nevertheless, a few high-entropy alloys have already been shown to possess exceptional properties, exceeding those of conventional alloys, and other outstanding high-entropy alloys are likely to be discovered in the future. Here, we review recent progress in understanding the salient features of high-entropy alloys. Model alloys whose behaviour has been carefully investigated are highlighted and their fundamental properties and underlying elementary mechanisms discussed. We also address the vast compositional space that remains to be explored and outline fruitful ways to identify regions within this space where high-entropy alloys with potentially interesting properties may be lurking.

[1]*Materials Science and Technology Division, Oak Ridge National Laboratory, Oak Ridge, TN, USA.*

[2]*Department of Materials Science and Engineering, University of Tennessee, Knoxville, TN, USA.*

[3]*Department of Microstructure Physics and Alloy Design, Max-Planck-Institut für Eisenforschung, Düsseldorf, Germany.*

[4]*Materials Sciences Division, Lawrence Berkeley National Laboratory, Berkeley, CA, USA.*

[5]*Department of Materials Science & Engineering, University of California, Berkeley, CA, USA.*

*e-mail: georgeep@ornl.gov; egeorge@utk.edu*

https://doi.org/10.1038/s41578-019-0121-4

Since the Bronze Age, humans have been altering the properties of materials by adding alloying elements. For example, a few percent by weight of copper was added to silver to produce sterling silver for coinage a thousand years ago, because pure silver was too soft. Examples from the modern era include steels that consist primarily of iron, to which elements such as carbon and chromium are added for strength and corrosion resistance, respectively, and copper alloyed with beryllium to make it strong and non-sparking for use in explosive environments. With few exceptions, the basic alloying strategy of adding relatively small amounts of secondary elements to a primary element has remained unchanged over millennia. It is even reflected in the way alloys are named after their principal constituent: ferrous alloys, aluminium alloys, titanium alloys, nickel alloys and so on. However, such a primary-element approach drastically limits the total number of possible element combinations and, therefore, alloys, most of which have been identified and exploited. New approaches are needed if the compositional space to explore is to be significantly enlarged.

One such approach is based on mixing together multiple principal elements in relatively high (often equiatomic) concentrations. This approach stands in sharp contrast to the traditional practice and has, therefore, attracted much attention. The related surge in research activity, especially during the past 5 years, can be traced back to the publication of two seminal papers[1,2] in 2004. Two groups independently proposed the study of a new class of alloys containing multiple elements in near-equiatomic concentrations. It was subsequently pointed out that conventional alloys tend to cluster around the corners or edges of phase diagrams, where the number of possible element combinations is limited, and that vastly more numerous combinations are available near the centres of phase diagrams, especially in quaternary, quinary and higher-order systems[3]. Owing to their sheer numbers, little is known about concentrated, multi-component alloys but, by the same token, because there are so many possible combinations, the concept offers promise to discover interesting new alloys with useful properties in their midst.

Jien-Wei Yeh and co-workers[1] provided an additional intriguing rationale for investigating these alloys: they hypothesized that the presence of multiple (five or more) elements in near-equiatomic proportions would increase the configurational entropy of mixing by an amount sufficient to overcome the enthalpies of compound formation, thereby deterring the formation of potentially harmful intermetallics. This was a counter-intuitive notion because the conventional view — likely based on binary phase diagrams in which solid solutions are typically found at the ends and compounds near the centres — was that the greater the number of elements in concentrated alloys, the higher the probability that some of the elements would react to form compounds. But Yeh and colleagues reasoned that, as the number of elements in an alloy increased, the entropic contribution to the total free energy would overcome the enthalpic contribution and, thereby, stabilize solid solutions (BOX 1; FIG. 1). They coined a catchy new name, high-entropy alloys (HEAs), for this

class of materials containing five or more elements in relatively high concentrations (5–35 at.%). Others have suggested alternative names, such as multi-component alloys, compositionally complex alloys and multi-principal-element alloys, as discussed elsewhere[4].

However, judging by its popularity in the literature, we suspect that, despite entropy not being the prime factor responsible for the structure and properties of these alloys, the term high-entropy alloys is likely to be the name that endures.

---

## Box 1 | Thermodynamics of phase stability

An alloy created by combining two pure elements A and B can form a solid solution or one or more intermetallic phases, depending on the relative free energies of the following reactions:

$$A + B = AB \text{ (solution)} : \Delta G_{mix} = \Delta H_{mix} - T\Delta S_{mix} \tag{1}$$

$$A + B = AB \text{ (intermetallic)} : \Delta G_f = \Delta H_f - T\Delta S_f \tag{2}$$

where $\Delta G_{mix}$, $\Delta H_{mix}$ and $\Delta S_{mix}$ are the Gibbs free energy, enthalpy and entropy of mixing, respectively; $\Delta G_f$, $\Delta H_f$ and $\Delta S_f$ are the corresponding values for the formation of an intermetallic compound with AB stoichiometry; and $T$ is the absolute temperature. If, instead, two intermetallic compounds with different stoichiometries form (such as $AB_2$ or $A_2B$), additional expressions similar to Eq. 2 are needed for each compound.

At thermodynamic equilibrium, the phases present in the alloy depend on whether the Gibbs free energy of mixing (Eq. 1) is more or less negative than the free energies of formation (Eq. 2) of all possible intermetallic compounds comprising the elements A and B (that is, $A_iB_j$, where $i, j = 1, 2, 3,…$) present individually or as mixtures. Note that it is not necessary for A + B to transform entirely into $A_iB_j$-type intermetallics; rather, intermetallics can precipitate within an A-rich or B-rich (terminal) solid solution, in which case the relevant free-energy change involves the sum of the free energy of mixing of the terminal solid solution and the free energy of formation of the intermetallic. Additionally, if intermetallic compounds are not favoured and only a solid solution forms, the solid solution need not be random (or ideal) because the different atomic species can cluster or order on the lattice, depending on whether $\Delta H_{mix}$ is positive or negative, respectively. Another possibility is that, instead of forming a single solid solution, the mixture decomposes into two solid solutions with different compositions, crystal structures and/or lattice parameters.

The situation becomes increasingly more complex as more alloying elements are added (A + B + C + …) because the number of possible phases that can co-exist correspondingly increases, as given by the Gibbs phase rule. If some of those phases are intermetallic compounds, they can be of several different types, even if we consider just the binary pairs (A–B, B–C, A–C, …). In reality, ternary and higher-order intermetallics, which need not all be line compounds, can also form, rapidly escalating the number of possibilities. In cases in which the compounds exhibit a compositional range of stability, the energies of the defects needed to accommodate deviations from stoichiometry (for example, anti-site defects) have to be accounted for. Some of the possible mixing reactions are shown in FIG. 1.

Even in simple A–B-type alloys, there is rarely complete miscibility across the entire composition range (from pure A to pure B). Rather, binary-phase diagrams typically exhibit solid solutions near the pure-element ends and a variety of intermetallic compounds in between, many of which are brittle. The problem is exacerbated in multi-element alloys, in which there are many more element pairs that can attract each other and, therefore, an increased number of potentially brittle intermetallics.

The traditional reluctance of metallurgists to work with concentrated, multi-element alloys was turned on its head by Yeh and co-workers[1], who proposed that the increased configurational entropy of mixing in alloys comprising multiple alloying elements (Eq. 1) would counteract the tendency for compound formation (Eq. 2). By adding more and more elements at near-equiatomic concentrations, it would be possible to stabilize solid solutions at the expense of intermetallics.

Yeh and co-workers[1] simplified the problem by assuming that the considered solid solution is ideal, in which case $\Delta H_{mix}$ in Eq. 1 is zero, and that the competing intermetallic compound is perfectly ordered, in which case $\Delta S_f$ in Eq. 2 is zero. The relative stabilities of the solid solution and intermetallic compound then depend on whether $-T\Delta S_{mix}$ (Eq. 1) is more negative than $\Delta H_f$ (Eq. 2). The ideal entropy of mixing is given by:

$$\Delta S_{mix} = -R\Sigma x_i \ln x_i \tag{3}$$

where $R$ is the gas constant and $x_i$ is the mole fraction of the $i^{th}$ element. In an equiatomic alloy, $x_1 = x_2 = x_3$ and so on, and the mixing entropy becomes:

$$\Delta S_{mix} = R\ln n \tag{4}$$

where $n$ is the number of elements in the alloy, yielding values for $\Delta S_{mix}$ of $1.39R$, $1.61R$ and $1.79R$ for equiatomic alloys containing 4, 5 and 6 elements, respectively.

Based on this simplification, they concluded that, in alloys with a high number of principal elements (say, $n = 5$), the entropic contribution to the free energy ($-T_m\Delta S_{mix}$) at the melting temperature $T_m$ is comparable to the formation enthalpies ($\Delta H_f$) of strong intermetallic compounds such as NiAl and TiAl, thereby suppressing compound formation, except those with large heats of formation, such as strong ceramic compounds (oxides, carbides, nitrides and silicides), and more easily yielding random solid solutions during solidification. Consequently, Yeh and co-workers defined high-entropy alloys as those with five or more elements in equiatomic concentrations. To allow for flexibility in alloy design, they relaxed the equiatomic requirement and permitted a range of concentrations from 5 to 35 at.% for each constituent element. However, this simple criterion based on the number of alloying elements is not sufficient to predict single-phase, solid-solution formation in multi-element alloys.
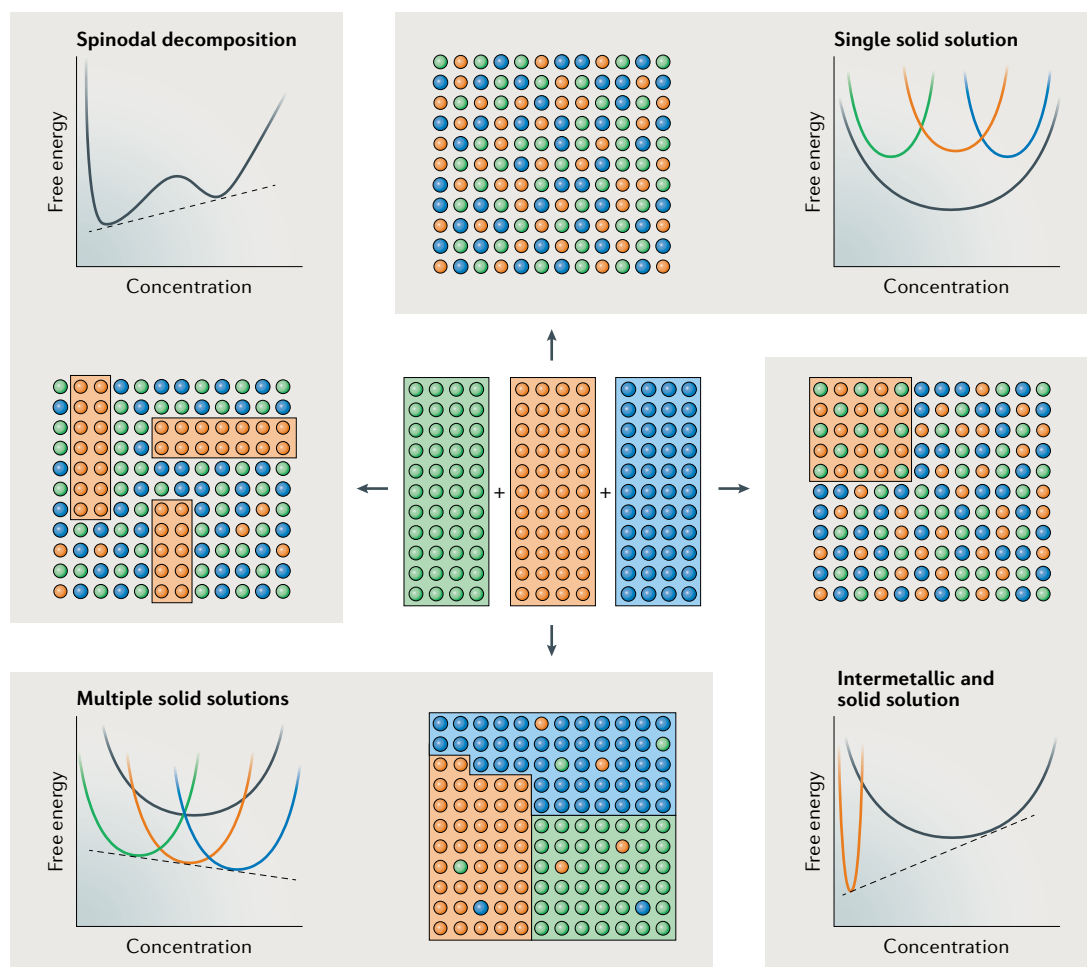
Fig. 1 | **Possible mixing reactions for three alloying elements.** Some of the possible reactions that can occur when three different elements, represented by the red, blue and green spheres, are mixed in equal proportions, including spinodal decomposition, formation of single or multiple solid solutions or precipitation of an intermetallic compound in a solid solution.

Interestingly, most of the HEAs investigated in the early years were multi-phase alloys rather than single-phase, solid solutions[5–10]. In recent years though, increased attention has been paid to a few model, single-phase alloys to probe their behaviour in greater detail and uncover fundamental mechanisms without the confounding effects of secondary phases. Investigation of single-phase alloys allows variables such as the number, types and concentrations of alloying elements to be systematically varied and directly correlated with physical and mechanical properties, such as elastic constants, stacking-fault energies, diffusion coefficients, strength and ductility. Such studies, although important in their own right, have broader applicability to the understanding of certain multi-phase alloys, such as the advanced γ–γ′ Ni-based superalloys used in jet engines and power generation, in which the matrix phase (γ) is a complex, solid solution consisting of multiple elements in relatively high concentrations, with none of them being the majority element[11]. At least some of the rate-controlling mechanisms that govern the overall properties of the γ–γ′ composite (such as dislocation climb) occur within the γ phase or at the γ–γ′ phase boundaries. Thus, a fundamental understanding of

the energetics and kinetics of point defects, dislocations and diffusion in complex solid solutions is relevant also to understanding the behaviour of multi-phase alloys (several defects and strengthening mechanisms are discussed in BOX 2). Finally, complex solid solutions are important from a basic scientific viewpoint because of the conceptual advances needed to bridge the gap between the relatively well understood dilute solid solutions and the poorly understood concentrated solid solutions.

In this Review, we present some approaches for efficiently probing the huge compositional space of HEAs for desirable structures and mechanisms that can help identify novel materials with interesting features. We first briefly reflect on some HEA success stories — there are not too many to date — using them as examples for discussing pertinent development strategies. Then, we discuss several specific pathways for the identification of new HEAs, namely, a thermodynamic pathway based on phase diagram calculations[12–19], an experimental combinatorial pathway[20–24] and a mechanistic pathway that aims at compositionally tailoring and combining specific microstructure mechanisms, such as twinning-induced plasticity (TWIP)[25–28] and transformation-induced

Box 2 | **Defects and strengthening mechanisms**

Real metals contain defects of various kinds that disrupt the regular 3D atomic structure of a perfect crystal. They can be classified as point defects (0D), line defects (1D), interface defects (2D) and volume defects (3D). Examples of point defects are vacancies, which enable diffusion in solids (missing atoms, panel **a** in the figure, in which they are shown with other defects), interstitials (atoms in the interstices of the crystal lattice) and substitutionals (atoms that substitute on the host lattice). As the figure shows, in high-entropy alloys (HEAs), it is difficult to distinguish between host atoms and substitutional solutes. Dislocations are line defects (panel **b** in the figure) and are the main carriers of plastic deformation in crystalline metals. They can be of the edge type (deformation normal to the dislocation line, as shown in the figure), screw type (deformation parallel to the dislocation line) or mixed. As panel **b** shows, shear by an amount equal to the magnitude of the Burgers vector on the slip plane creates an extra half-plane of atoms and an edge dislocation. Interface defects include grain boundaries, which separate regions of different orientations in a polycrystalline material (panel **a**); twin boundaries, which separate regions that are mirror images of each other created by shear parallel to the twin planes (panel **c** in the figure; in face-centred cubic crystals, the twin planes are of the {111} type and the twinning shear is along the <112> directions); stacking faults, in which the normal stacking sequence of certain planes is disrupted; phase boundaries, which separate different phases in a material; and surfaces on which the solid is exposed to (often harsh) environments. Examples of volume defects are precipitates (panel **a**), inclusions and voids. Defects such as vacancies, stacking faults, twins and dislocations disrupt the local structure of a pure metal, whereas in multiple-element, concentrated solutions, including HEAs, they also disrupt the local chemistry. This makes it considerably more difficult to investigate, both experimentally and computationally, the energetics and kinetics of defects. The chemical complexity of HEAs also introduces conceptual difficulties: in dilute alloys, the host element is the solvent into which the solutes dissolve, but in equiatomic HEAs, there is no clear way to distinguish between solvent and solute.

Plasticity requires the movement of dislocations through the metal (panel **d** in the figure). Anything that hinders this motion makes the material stronger (harder to deform plastically). Many of the defects mentioned above can act as obstacles to dislocation motion, including alloying elements, vacancies (at relatively low temperatures), twin boundaries, grain boundaries and phase boundaries. Certain twin boundaries allow the partial dislocations to glide along their interfaces, thereby relieving some of the stresses built up by the dislocation pile-up and enhancing ductility. Panel **d** shows schematically how dislocations are held up at precipitates and solutes, and grain and twin boundaries. In simple terms, the strengthening due to obstacles varies inversely with their spacing and directly with their 'strength', that is, the force (energy) required to break through. Thus, closely spaced, strong obstacles produce the most strengthening. As in conventional metals, each of the above strengthening mechanisms has been employed to strengthen HEAs. However, unlike in conventional metals, in which strengthening is invariably accompanied by a loss of ductility and toughness, in some HEAs this trade-off can be avoided, as it appears that certain (unknown) characteristics of twin and phase boundaries make certain HEAs less apt to become brittle when their strength is increased. A fundamental understanding of the reasons for this behaviour is critical for the mechanistic design of stronger and tougher materials.
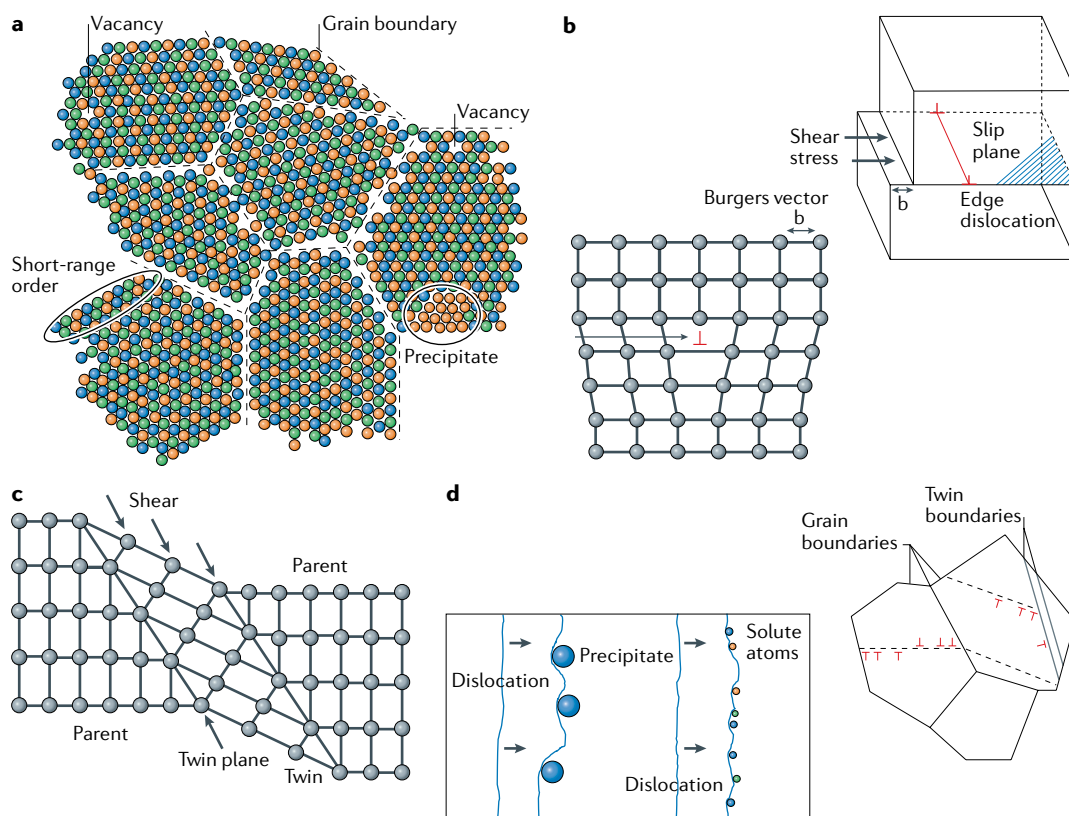
plasticity (TRIP)[29–31]. We conclude by discussing prospects and future opportunities for the field, highlighting theoretical and experimental tools that should be developed to identify new HEAs and the directions that should be the focus of future research, including developing HEAs that work well at high temperature and HEAs that display combinations of properties and functionalities that are not found in existing materials.

## Single-phase, high-entropy alloys
### Phase stability and configurational entropy
The appeal of the entropy hypothesis[1] lies in its straightforward, testable prediction: alloys comprising five or more elements would form single-phase solid solutions. However, when put to the test[32], it turned out that, in several nominally similar, five-element alloys, all of them except for one contained multiple intermetallic phases, showing that configurational entropy is not a useful predictor of which alloys are simple solid solutions. In addition to configurational entropy, one needs to take into account other entropic contributions, as well as mixing enthalpies[32–35]. A further complication was that Yeh and co-workers' analysis was performed at the melting point, whereas most alloy microstructures tend to be examined at room temperature. Depending on diffusion rates, phase-transformation kinetics and cooling rates, room-temperature and high-temperature microstructures may be quite different. Indeed, HEAs often contain multiple phases when examined at room temperature, and many of the second phases are intermetallics that can be brittle and hinder mechanical performance. If the goal is to avoid the formation of such phases, simply mixing together five or more elements in near-equiatomic concentrations is unlikely to be a useful approach. Even multi-component alloys that are initially single phase after solidification tend to separate into multiple metallic and intermetallic phases when annealed at intermediate temperatures[36–40]. This phase instability has only recently been recognized as a common feature of many (perhaps most) HEAs and needs to be accounted for when considering alloys for high-temperature applications.

Because phase relationships are governed by the total free energy, the original high-entropy criterion could conceivably be supplemented with a 'low-enthalpy' criterion for solid-solution stability. In fact, there are many alloys containing fewer than five elements (medium-entropy alloys) that are single-phase solid solutions; these alloys may well be enthalpy-stabilized rather than entropy-stabilized. This relaxes the original high-entropy criterion that alloys should contain five or more elements in near-equiatomic ratios. It also provides a wider composition space for investigation that includes alloys with fewer elements, as well alloys deviating from equiatomic compositions[27,41]. However, determining the enthalpy is not as easy as estimating the configurational entropy of an ideal solid solution. Therefore, although one could christen these alloys 'low-enthalpy alloys', it is less useful as a classification scheme.

Given the importance of predicting and understanding the microstructures of HEAs, several studies have attempted to treat the thermodynamics of phase stability in complex alloys more fully, with varying degrees of success. Truly ab initio calculations are tedious, especially at finite temperatures[34,42,43]. Thus, they are probably best suited to screening narrow composition ranges that have already been identified as being of interest (based on other considerations) and when phase stabilities need to be predicted accurately. Calculation of phase diagrams (CALPHAD)-type approaches, which use software to calculate phase diagrams based on thermodynamic models, in general have broader applicability and have been shown to be useful in predicting phase stability in some cases[13,17,44,45].

Numerous other studies, summarized elsewhere[4,46–48], have attempted to relate phase stability to parameters such as size misfits, valence electron concentrations, electronegativities and mixing enthalpies. However, many of these treatments ignore the formation enthalpies of competing compounds, typically intermetallic phases, which, in our view, limits their usefulness. The typical procedure is to construct empirical 'phase stability maps' as functions of the above parameters. 'Critical' values for the parameters are then estimated, above or below which certain types of microstructures (such as solid solutions) are stable. These values appear to be arbitrary and based on back-tested correlations, with little evidence of predictive capability. Other thermodynamically more consistent approaches[49–51] have identified suitable compositional subspaces where single-phase HEAs might exist by additionally considering the enthalpies of competing intermetallic compounds. However, they also suffer from the drawback that 'arbitrary' values of formation enthalpies of competing compounds have to be used to 'predict' regions where single or multiple phases are stable.

In this connection, it is worth noting that, in many studies, minimal effort is put into determining the reliability of the experimental observations used for the correlations described above. For example, as described in previous reviews[4,52], many studies rely on X-ray diffraction (XRD) alone to determine the microstructural states of the alloys investigated, which has the potential of mistakingly identifying an alloy as a single-phase solid solution, because the technique only provides spatially averaged information and cannot detect small amounts of secondary phases that may be present. Nevertheless, given the vastness of the compositional space that HEAs occupy, such low-resolution techniques are probably unavoidable to perform a rough initial screening to identify which compositions might be worth investigating in further detail.

### Notable high-entropy alloys
Single-phase, solid-solution HEAs with face-centred cubic (FCC)[2,25,32,41,53–68], body-centred cubic (BCC)[69–78], hexagonal close-packed (HCP)[79–83] and orthorhombic[84] crystal structures have been identified. Of these, the FCC and BCC alloys are by far the most extensively investigated; thus, we limit our discussion to these two crystal structures. Within them, we focus on a few model HEAs whose structure–property relationships have been carefully studied to uncover salient features of their behaviour.

***The FCC CrMnFeCoNi (Cantor) alloy.*** The quinary CrMnFeCoNi alloy was one of the first equiatomic HEAs reported to crystallize as a single-phase FCC solid solution[2]. However, it was later discovered[38] that it decomposes into metallic (BCC-Cr) and intermetallic ($L1_0$-NiMn and B2-FeCo) phases below about 800 °C. Some of these transformations occur very quickly when the alloy is in the nanocrystalline state[36] but take longer in large-grained material[37,67]. It is not known whether this difference is due to the grain boundaries providing favourable nucleation sites and/or faster diffusion paths. Regardless, after heat treatments above 800 °C, the metastable FCC, solid-solution state can be retained at room temperature at 'normal' cooling rates. Its microstructure has been examined at multiple length scales using XRD[32,53,85–87], scanning electron microscopy[38,53,58,63], transmission electron microscopy (TEM)[25], electron backscatter diffraction[58,63] and atom probe tomography[36,62]. Taken together, the results show that the alloy is a single-phase, FCC, solid solution with no indication of clustering or short-range ordering, although if such local ordering were experimentally proven to exist, density functional theory (DFT) calculations suggest that it would have a profound effect on critical properties such as the stacking-fault energy and dislocation mobility, and, thus, it would be a major factor in controlling mechanical properties[88]. After deformation processing and recrystallization, the crystallographic texture is weak and close to random[64]. At very low temperatures, below about 50 K, computations based on DFT show that the FCC structure of the Cantor alloy becomes unstable and transforms to the HCP structure[34]. There has been no direct experimental confirmation of this temperature-induced phase transformation but two experimental studies indicate a pressure-induced transformation from FCC to HCP[89,90].

Although the discovery of the Cantor alloy dates back to 2004, it was not until almost a decade later that its malleability began to be appreciated and exploited. This enabled thermomechanical processing and, consequently, tensile tests to be performed for the first time on a polycrystalline HEA with well-controlled microstructure[53]. Several important features of the Cantor alloy were revealed[53]: this alloy exhibits a strong temperature dependence of strength below 473 K, a weaker temperature dependence at elevated temperatures up to 1,273 K and a modest strain-rate dependence at low homologous temperatures; its strength and ductility both increase with decreasing temperature down to the cryogenic range, with ultimate strengths and elongations in excess of 1 GPa and 60%, respectively, at 77 K; its work-hardening rate increases strongly with decreasing temperature, which postpones the onset of necking and, thereby, increases the tensile ductility; and it fractures transgranularly by ductile microvoid coalescence, which is consistent with the high ductilities observed. As discussed later in this section, tests on single crystals of the Cantor alloy have confirmed the temperature dependence of yielding observed in polycrystalline samples.

Subsequent investigations characterized the dislocation structures and microstructural evolution with strain to obtain a fundamental understanding of the mechanical properties of the Cantor alloy. Multiple deformation mechanisms appear during tensile tests. The main findings at room temperature are that slip initially occurs by planar glide of 1/2<110> dislocations on {111} planes[25,64,91]. The perfect dislocations split into 1/6 <112> Shockley partial dislocations bounding a stacking fault with average splitting distances ranging from ~3.5–4.5 nm for the edge orientation to ~5–8 nm for the screw orientation, yielding a stacking-fault energy of 30 ± 5 mJ.m$^{-2}$ (REF.[91]). This experimental stacking-fault energy is slightly greater than the 0 K value computed using DFT techniques (18–27 mJ.m$^{-2}$)[92]. The relatively large partial separations (especially when normalized by the Burgers vector) imply that cross slip is difficult in this alloy, which is consistent with the planar slip and long dislocation pile-ups observed at grain boundaries[25]. At high magnifications, significant (by a factor of 2) local variations in the stacking-fault widths are observed[93], which could be due to local changes in the stacking-fault energy related to local variations in composition. At lower magnifications, the dislocations are long and smoothly curved on the {111} planes without any preferred line direction, implying similar mobilities of edge and screw segments[91]. In situ straining experiments in TEM[94] suggest that the Shockley partials are more mobile than the perfect (undissociated) segments, which are very sluggish; the fast-moving partials are arrested at the planar slip bands consisting of perfect dislocations. However, because no information regarding the locally resolved shear stress acting on the moving dislocations was available, caution has to be exercised in drawing conclusions about the relative mobilities of the different dislocations seen during such in situ observations.

With increasing strain at room temperature, partials are activated on multiple-slip systems, and those moving on inclined slip planes interact at their junctions; some of these interactions produce 3D parallelepiped volume defects that act as further barriers to planar slip[94], analogous to the stacking-fault tetrahedra seen in FCC metals. The dislocation density increases from very low values in the recrystallized (unstrained) state to 2–4 × 10$^{14}$ m$^{-2}$ at strains of 15–20%[64]. Eventually, well-developed cell structures form at strains of 20% or higher[25,64]. The work-hardening rate decreases rapidly from ~$G/20$ (where $G$ is the shear modulus) at the start of tensile straining to ~$G/30$ at approximately 8% true strain; beyond that, the work-hardening rate continues to decrease, but less rapidly, reaching ~$G/10$ at 30% strain[64]. Thus, as in other FCC metals and alloys, dislocation mechanisms by themselves are insufficient to sustain a steady (non-decreasing) work-hardening rate. At high applied stresses close to the fracture stress, twinning is finally activated[64], but it appears too late in the deformation process to prevent the onset of necking instability.

The microstructure evolution is distinctly different when the straining is carried out at cryogenic temperatures. At 77 K, the distribution of dislocations and their density evolution with strain is initially similar to that at room temperature[64]. Correspondingly, the work-hardening rate decreases rapidly from ~$G/20$ at the start of tensile straining to ~$G/30$ at approximately 8% strain. However, beyond that, twinning is activated, which

provides an additional hardening mechanism. Thus, work hardening remains constant at ~$G$/30 for true strains from 8% to almost 40%[64]. The twins have nanoscale widths (~10–25 nm on average) and micrometer-scale spacing (mean values ranging from ~20 μm at 8% strain to ~1 μm at 45% strain)[64]. Assuming that the twin boundaries act like grain boundaries as barriers to dislocation motion, the decrease in twin spacing with strain is indicative of a dynamic Hall–Petch effect that provides hardening to counteract the softening due to dislocation recovery processes. This additional hardening mechanism maintains a constant, steady, work-hardening rate at strains at which dislocation hardening peters out.

Based on TEM investigations of samples taken from interrupted mechanical tests, twins were found to appear at true strains of ~7.5% at 77 K, but at much higher strains (~25%, close to fracture) at room temperature[64]. The corresponding tensile stresses were ~720 MPa at both temperatures, indicative of a temperature-independent twinning stress similar to what has been seen in many other materials[95]. Dividing the polycrystalline twinning stress by the Taylor factor gives a critical resolved shear stress (CRSS) for twinning of about 235 MPa. The RSS is the component of the applied stress acting on the slip plane in the slip direction and its critical value (CRSS) is the one at which twinning (or slip) is initiated. The above CRSS value has to be treated with caution because the polycrystalline material investigated had a relatively small grain size of 17 μm (REF.[64]), and it is known that twinning becomes more difficult as the grain size is decreased[95]. A better estimate could be obtained by testing materials with larger grains. Furthermore, there are experimental uncertainties related to where in the gauge section the TEM specimens are taken from and the limited volume examined by TEM (twinning may well have occurred at lower strains, but the sampling may have been insufficient to catch it).

Single crystals offer a more direct way to characterize twinning in the Cantor alloy[96–100]. From a [111]-oriented tensile specimen, the CRSS value for {111}<112> twinning was determined to be ~150 MPa at 77 K and it occurred on the twin system with the highest Schmid factor[96]. Another [111] specimen tested at room temperature did not exhibit twinning, although it work-hardened extensively and experienced a stress higher than the twinning stress at 77 K. This latter observation suggests the possibility that the twinning stress may indeed depend on temperature, although to what extent remains unknown. Two other orientations were tested at 77 K but they did not show twinning because the applied stress did not reach the twinning stress.
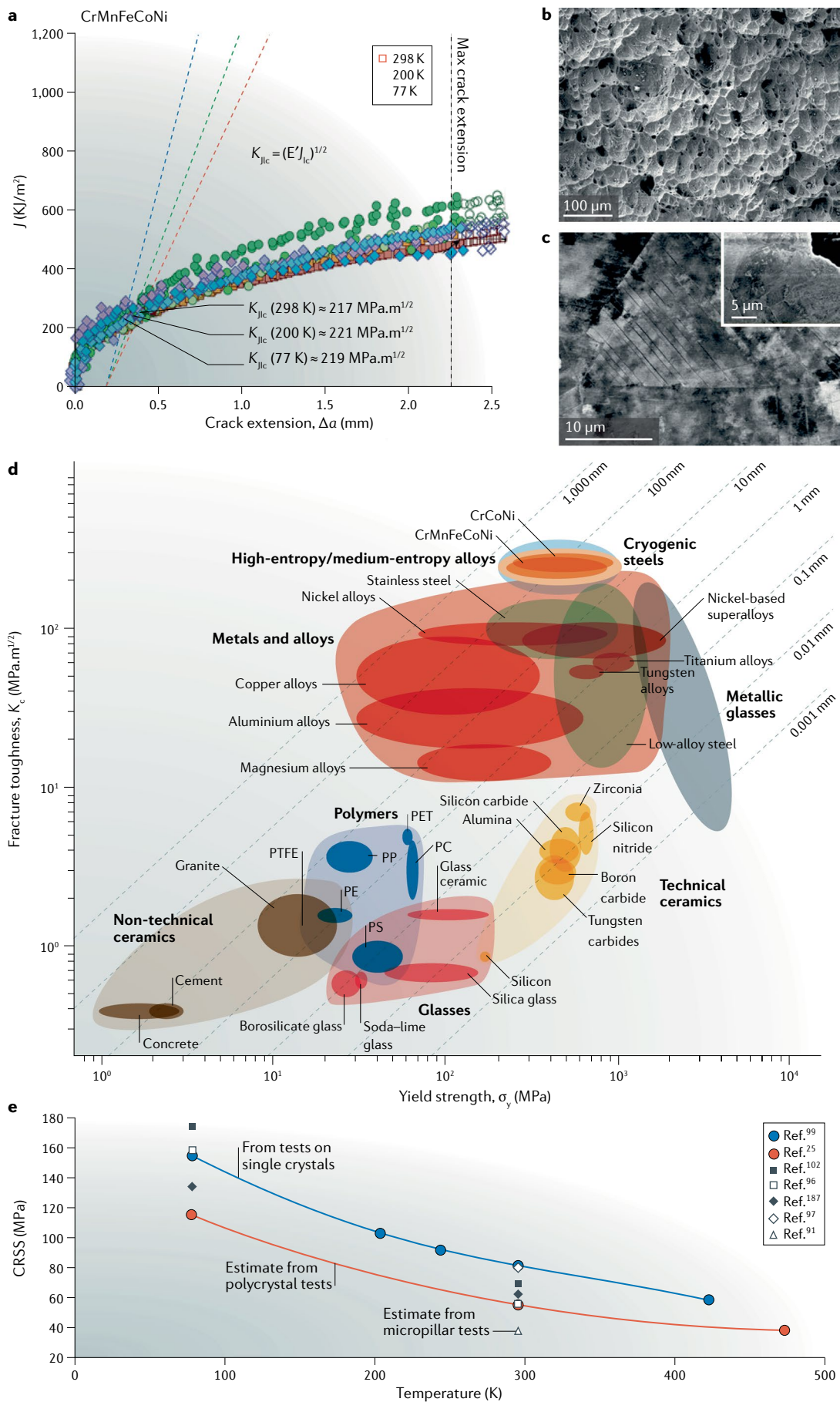
Consistent with its high strength and ductility, the Cantor alloy exhibits exceptional fracture toughness[57] (FIG. 2): its crack-initiation toughness ($K_{\text{JIc}}$) is ~220 MPa.m$^{1/2}$, roughly independent of temperature from room temperature down to 77 K, whereas its crack-growth toughness exceeds 300 MPa.m$^{1/2}$ at these temperatures (rising $R$-curve behaviour; that is, increasing resistance to cracking as the crack length increases). Whereas an increase in strength and ductility with decreasing temperature is seen in other FCC alloys (for example, austenitic stainless steels), the retention of high

toughness at cryogenic temperatures makes the Cantor alloy unique, because most materials become more brittle as the temperature is decreased. Twinning was observed in the highly stressed regions in front of the crack tip in fracture toughness specimens tested at 77 K. In a follow-up in situ TEM straining study, twinning was observed in the crack-bridging ligaments behind the crack tip at room temperature[94]. Twinning has also been observed in the Cantor alloy after high-pressure torsion[36] and rolling[101], both of which subject the material to high strains and stresses.

From compression tests on a [$\bar{5}$91]-oriented single crystal, the CRSS for the activation of {111}<110> slip in the Cantor alloy was first determined to be 70 MPa and 175 MPa at room temperature and 77 K, respectively[102]. These values are higher than those estimated by dividing the polycrystalline yield stress by the Taylor factor: for example, for a grain size of 155 μm, the yield stresses at room temperature and 77 K are ~170 MPa and 350 MPa, respectively[25], from which upper limits of the corresponding CRSS can be deduced as ~55 MPa and 114 MPa, respectively. Single-crystal, micropillar compression results[91] showed that the extrapolation of size-dependent strengths to pillar sizes of 20–30 μm gave values for the bulk CRSS of 33–43 MPa at room temperature that are more in line with the polycrystalline data. Additionally, the CRSS values were not orientation dependent (Schmid's law was valid for the [$\bar{1}$26] and [$\bar{1}$23] orientations tested). Subsequently, [111]-oriented, [149]-oriented, [122]-oriented and [123]-oriented single crystals were tested in tension and CRSS values of ~55 MPa and 150 MPa were obtained at room temperature and 77 K, respectively, again independent of orientation[96]. As was the case for the yield strengths of polycrystals[25,53], the single-crystal data show that the CRSS increases significantly as the temperature is decreased from room temperature to 77 K (FIG. 2e, blue curve). As can be seen in the figure, there are noticeable differences between the CRSS obtained directly from single-crystal tests and those obtained indirectly from polycrystal tests (FIG. 2e, red curve) or micropillar compression tests (FIG. 2e, open triangle), which may be related to the approximations inherent in the indirect methods. However, the CRSS from several single-crystal studies (other symbols in FIG. 2e) are also different from the blue curve, which may be due to compositional variations or impurity effects.

A question that naturally arises is whether the temperature dependence of the CRSS (or of the yield or flow strength of polycrystals) is owing to the temperature dependence of the shear modulus $G$, given that strength is proportional to $G$. However, $G$ of the Cantor alloy shows a relatively weak temperature dependence[60], weaker than that of pure Ni, in the temperature range from room temperature down to 77 K, at which the yield strength of the Cantor alloy increases dramatically, whereas that of Ni is relatively flat. Therefore, the temperature dependence of $G$ cannot be the reason for the temperature dependence of the CRSS.

Although the strong temperature dependence of the CRSS of the Cantor alloy between room temperature and 77 K stands in sharp contrast to the behaviour of

**a**



CrMnFeCoNi

$K_{Jlc} = (E'J_{lc})^{1/2}$

$K_{Jlc}$ (298 K) ≈ 217 MPa.m$^{1/2}$

$K_{Jlc}$ (200 K) ≈ 221 MPa.m$^{1/2}$

$K_{Jlc}$ (77 K) ≈ 219 MPa.m$^{1/2}$

**b**



**c**



**d**



**e**

◀ Fig. 2 | **Damage-tolerant properties of the Cantor CrMnFeCoNi alloy. a** | Fracture toughness, crack resistance curves show that the Cantor alloy displays a fracture toughness at the point of crack initiation, $K_{Jlc}$, in excess of 200 MPa.m$^{1/2}$ from ambient temperature down to liquid-nitrogen temperature, and valid crack-growth toughnesses above 300 MPa.m$^{1/2}$. Note that the $J$ integral is a fracture-mechanics characterizing parameter that represents a measure of the stress and displacement fields in the vicinity of the crack tip. **b, c** | Such exceptional toughness properties, which are even higher in the three-component CrCoNi alloy, are associated with (panel **b**) a fully ductile microvoid coalescence mode of fracture, as shown by the scanning electron microscope image, and (part **c**) extensive deformation nano-twinning at 77 K, as seen from the backscattered electron micrograph (the roughly 10% stronger CrCoNi alloy deforms by twinning at temperatures as high as 293 K). **d** | Ashby plot of strength versus fracture toughness showing that CrCoNi-based, medium-entropy and high-entropy alloys are among the most damage-tolerant materials on record. **e** | Critical resolved shear stress (CRSS) for slip at different temperatures derived from tests on single crystals; also shown are values estimated from tensile tests on polycrystals and micropillar compression tests. PC, polycarbonate; PE, polyethylene; PET, polyethylene terephthalate; PP, polypropylene; PS, polystyrene; PTFE, polytetrafluoroethylene. Panels **a**, **b** and **c** are adapted with permission from REF.[57], AAAS. Panel **d** is adapted with permission from REF.[57], AAAS, and REF.[116], CC-BY-4.0.

pure FCC metals such as Ni, it is well known that solid-solution alloys, including binaries[103–108], exhibit temperature dependences that increase with increasing solute concentration. A new theory of solid-solution strengthening developed for concentrated alloys[109,110] quantitatively explains the temperature dependence of strength observed in the Cantor alloy and its FCC subsets[59].

The room-temperature CRSS at yield of the Cantor alloy is an order of magnitude larger than that of Ni (~3 MPa (REF.[111])), which is an FCC metal with comparable melting point and shear modulus. This degree of solid-solution strengthening cannot be reconciled in terms of the maximum difference (~1%) in the atomic (Goldschmidt) radii of the constituent elements. However, the effective atomic radii in the Cantor alloy can be calculated using DFT methods, and the maximum (pair-wise) size difference turns out to be ~4%[91]. Based on this, a hypothetical binary alloy with 4% mismatch, the shear modulus of the Cantor alloy and a solute concentration in the range 20–50% was shown to have yield strengths comparable to that of the Cantor alloy[91]. Because the constituent elements have different atomic sizes, their centres are displaced from the ideal FCC lattice points. The displacement of each element can be calculated using DFT methods[112] and it depends on the local environment (that is, surrounding atoms). The computed mean square atomic displacement is largest for Cr (~43 pm$^2$) and smallest for Ni (~9 pm$^2$). Averaging the computed mean square atomic displacements over the entire crystal gives a value of 25 pm$^2$ for the Cantor alloy. Experimentally, the atomic displacement of the individual elements is difficult to measure. However, using synchrotron XRD, the atomic displacement parameter, which is the sum of the squares of the atomic displacements averaged over the entire crystal, was determined to be ~24 pm$^2$ and 59 pm$^2$ at 25 K and 300 K, respectively[112]. The atomic displacement parameter value at 25 K is representative of the static disorder in the Cantor alloy, whereas the difference between it and the room-temperature value is representative of the dynamic disorder due to thermal vibrations. The 25 K value is almost identical to the computed value (average

of mean square atomic displacements) and its square root gives the average displacement of the atoms in the Cantor alloy from their ideal lattice positions, namely ~5 pm. This gives a sense of the average lattice distortion (<2% of the Burgers vector) needed to obtain significant, solid-solution strengthening in the Cantor alloy. Of course, the displacements of the individual atoms can be larger (~6.5 pm for Cr and ~5.5 pm for Mn), smaller (~4 pm for Co and ~3 pm for Ni) or similar (~5 pm for Fe) to the displacement averaged over the whole alloy[112].

*Non-equimolar and multi-phase derivatives of the Cantor alloy.* Based on the equimolar Cantor alloy, several related variants with fewer alloying elements or non-equimolar compositions have been developed. One of the rationales was to reduce the stacking-fault energy to promote TWIP[26,27] and/or TRIP[29,30] and, thus, to realize materials with superior strain-hardening potential.

One effective approach has been to simply remove elements from the Cantor alloy, the most notable examples being the equiatomic, medium-entropy alloy CrCoNi (REFS[59,113,114]) and the related ultrastrong alloy VCoNi (REF.[115]). These single-phase FCC alloys appear to be similar to the five-element Cantor alloy, only with enhanced strength and ductility[59,115] and toughness[116]. Indeed, at 77 K, CrCoNi (with 5–50-μm grain size) displays tensile strengths approaching 1.4 GPa, tensile ductilities of ~90% and fracture toughness values of ~270 MPa.m$^{1/2}$ at crack initiation and exceeding 400 MPa.m$^{1/2}$ for crack growth, making it one of the most damage-tolerant materials on record[116]. Its lower stacking-fault energy and higher yield strength (compared with the Cantor alloy) allows it to reach the twinning stress more easily, resulting in profuse nano-twinning, even at room temperature[117]. The twin boundaries act to arrest dislocations that impinge upon them and promote strength, yet the boundaries themselves act as pathways for the glide of partial dislocations, thus promoting ductility[113]. Significant increases in the yield strength of the single-phase CrCoNi alloy to values exceeding 1 GPa have been achieved by cold work followed by partial recrystallization[118,119], albeit at the sacrifice of tensile ductility (which decreased to 20–30%). Precipitation of a second phase with the $L1_2$ crystal structure can also enhance the yield strength of CrCoNi (to ~800 MPa, somewhat lower than that obtained by cold work) while maintaining a tensile ductility in excess of 40%[114]. However, because the precipitate type, volume fraction and size distribution have not been optimized, there is room to further enhance the strength–ductility combination of CrCoNi-based alloys.

Another approach[26,120–122] involved developing a non-equiatomic $Fe_{40}Mn_{40}Co_{10}Cr_{10}$ HEA that deformed by planar dislocation slip early on and by mechanical twinning at larger strains (>10%) at room temperature. In the equimolar Cantor alloy, such TWIP has only been observed under cryogenic conditions or after the application of very high strains, as discussed before. A group of novel, non-equiatomic, multi-component CrMnFeCoNi alloys that form planar slip substructures at strains <2% and complex cell structures with high dislocation-density walls at higher strains (up to 45%) was also developed[123]. Its strain-hardening properties

were similar to those of the Cantor alloy but it used lower-cost alloying elements.

Experiments on a set of Cantor-related HEAs with composition $Fe_{80-x}Mn_xCo_{10}Cr_{10}$, where the Mn content was varied between $x = 30$ at.% and 45 at.%[29] (FIG. 3), showed that, whereas the Mn-rich alloy (45 at.%) deforms by the development of complex dislocation patterns, the 40 at.% Mn variant is a TWIP alloy and the 35 at.% Mn variant is a TRIP alloy, reflecting the influence of the reduction in stacking-fault energy with decreasing Mn content. The 30 at.% Mn variant is an alloy consisting initially of two HEA phases, an FCC and an HCP phase (FIG. 3). As both phases are massive solid solutions, the alloy was termed dual-phase HEA. The FCC phase is metastable, so it partially transforms into HCP martensite upon loading. Alloys consisting of two such (metastable) HEA phases, notably FCC and HCP, are characterized by a near-zero stacking-fault energy. This feature was recently shown to enable not only a forward TRIP effect from the FCC to the HCP phases but also local reverse transformation back into the FCC phase. This mechanism, which seems to proceed through the forward and backward motion of individual partial dislocations, was referred to as the bidirectional TRIP (B-TRIP) effect, and it substantially refines the microstructure down to a nanolaminate-type substructure[124]. The associated high interface density reduces the dislocation's free path, hence enhancing the strength of the material (BOX 2).

Alloy variants that undergo a similar sequential activation of athermal, deformation-driven transformations to provide additional strain hardening have also been realized through interstitial alloying[121,122,125], using knowledge from TWIP and TRIP steels.

These examples of Cantor alloy variants demonstrate that modest deviations from the equimolar compositions originally prescribed for HEAs can be used for compositional tuning of the stacking-fault energy. Through this approach, thermodynamically guided strain-hardening engineering can be accomplished, enabling the activation of beneficial strain-hardening features, including stacking faults, reactions among partial dislocations, complex dislocation patterns, twinning and martensite formation.

*The BCC TiZrHfNbTa alloy.* Compared with the extensive information available on the FCC Cantor alloy and its derivatives, little is known about the fundamental structure–property relationships in BCC HEAs, especially the refractory HEAs, which we refer to as Senkov alloys because of Oleg Senkov's leading role in identifying and developing them. The paucity of data on refractory HEAs is mainly due to their brittleness and high melting points, which make it difficult to break down their cast, dendritic microstructure and produce material with homogeneous structure and composition[69,71]. The exception is the equiatomic Senkov alloy TiZrHfNbTa, which is the only one that exhibits tensile ductility at room temperature[75,126]. It was first synthesized in 2011 by arc melting followed by hot isostatic pressing, after which it had a dendritic microstructure[72]. XRD studies indicated that it was mostly single-phase BCC with one minor extra peak that the authors thought belonged to a hexagonal phase[72]. The lattice parameter of the BCC phase was determined to be 0.3404 nm, close to the 0 K value computed by DFT methods of 0.339 nm (REF.[127]). Subsequent research[128] looked at the alloy after arc and induction melting in a water-cooled Cu crucible and found only BCC peaks in the XRD spectrum, which



Increasing Fe content

Increasing stacking-fault energy

High-entropy alloy (45% Mn)

**TWIP** High-entropy alloy (40% Mn)

**TRIP** High-entropy alloy (35% Mn)

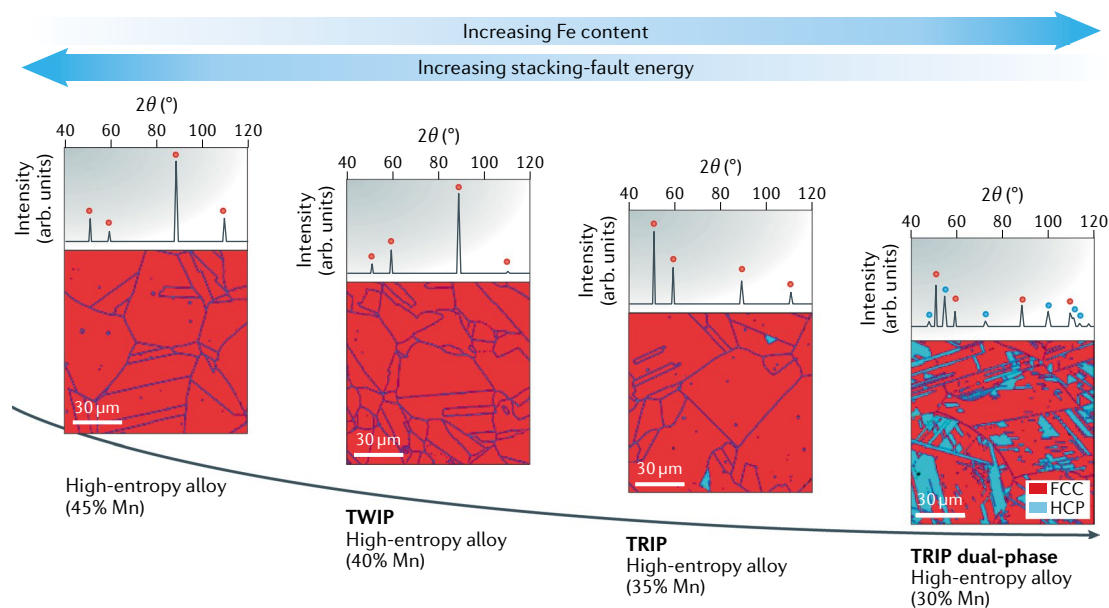**TRIP dual-phase** High-entropy alloy (30% Mn)

■ FCC
■ HCP

Fig. 3 | **Tuning the stacking-fault energy and the phases in a set of non-equimolar derivatives of the Cantor alloy.** The phase fractions (red, face-centred cubic, FCC; blue, hexagonal close-packed, HCP) for the alloy system $Fe_{80-x}Mn_xCo_{10}Cr_{10}$ change as a function of Mn content. The associated dominant deformation mechanisms are indicated. The spectra above the microstructure images show X-ray diffraction signals in which the peaks identify the respective phase fractions probed over millimetre-sized sample regions. TRIP, transformation-induced plasticity; TWIP, twinning-induced plasticity. Adapted from REF.[122], CC-BY-4.0.

yielded a comparable lattice parameter of 0.3401 nm. The alloy had a dendritic microstructure near the surface that was in contact with the Ar atmosphere (where the cooling rate was relatively slow), which disappeared near the surface in contact with the Cu (where the cooling rate was high). The dendrite arms were enriched in Ta and Nb (which have the highest melting points), whereas the interdendritic regions were enriched in the elements with lower melting point, Ti, Zr and Hf. The solidification zone that was devoid of dendrites appeared to be free of segregation. TEM analysis confirmed that the alloy was single-phase BCC at the microscopic scale[128]. Similar dendritic segregation was observed in another study[129], which also reported a comparable lattice parameter (0.3414 nm).

The cast TiZrHfNbTa alloy was tested initially in compression from room temperature to 1,473 K (REFS[72,73]) and then in tension at room temperature[126]. Depending on the location within the casting from where the tensile specimens were cut, significant variations in the room-temperature, tensile stress–strain curves were observed[126], which was ascribed to the different degrees of dendritic segregation and other casting defects, such as porosity, in the different regions. Yield strengths ranged from 790 MPa to 805 MPa, followed by modest strain hardening[126]. It appeared that regions exhibiting a greater degree of dendritic segregation were slightly stronger[126], but the limited available data makes it difficult to draw robust conclusions. Tensile ductilities ranged from ~6% to 9% and showed no clear correlation with strength[126], suggesting that the influence of casting defects may be dominant. Before fracture, specimens exhibited necking and post-rupture examination showed that the fracture surface was transgranular and covered in dimples of various sizes[126]. TEM analysis after interrupted compression tests revealed that, at small strains, deformation was localized in small bands bounding dislocation-free regions[130]. With increasing strain, the number of bands and the dislocation density in the bands increased. X-ray line profile analyses yielded values for the dislocation density of $1.5 \times 10^{15}$ m$^{-2}$ at compressive strains of 20%. The Burgers vectors were of the 1/2<111> type and the dislocations became more screw-like with increasing strain[130], indicating that their mobilities were lower than those of edge dislocations, similar to observations in other BCC metals (in which the usual reasoning is that the faster-moving edges exit the specimen, leaving behind the sluggish screws). Consistent with the Peierls mechanism and a strong intrinsic lattice resistance, the activation volume for plastic deformation obtained from room-temperature, stress-relaxation experiments was around $50b^3$ at yield, and decreased slightly to around $30b^3$ at 20% plastic strain[77], where $b$ is the magnitude of the Burgers vector. For comparison, the FCC Cantor alloy has a much larger activation volume at a yield of $\sim350b^3$, which decreases to $\sim150b^3$ at ~20% plastic strain[66].

A major advance in the study of BCC HEAs was the discovery that the TiZrHfNbTa Senkov alloy can be heavily cold rolled (~86% thickness reduction) and recrystallized[75], which opened the door to thermomechanical processing and grain-size control[131]. Tensile tests on

material with ~30-μm grain size gave a yield and ultimate stress of 1,145 MPa and 1,262 MPa, respectively, and an elongation to fracture of 9.7%[75]. The fracture mode was mainly intergranular, but regions of ductile transgranular fracture were also observed[75]. A subsequent study[131] investigated larger grain sizes of 38 μm, 81 μm and 128 μm and obtained yield strengths of 958 MPa, 944 MPa and 940 MPa, respectively. The Hall–Petch line drawn in that study, if extrapolated to smaller grain sizes, falls significantly below the yield strength of 1,145 MPa previously reported[75]. Additional work is needed to understand the reason for the discrepancy between these two studies. Elongations to fracture of 15%, 18% and 20% for grain sizes of 128 μm, 81 μm and 38 μm, respectively, were reported, which is consistent with the textbook notion that grain refinement can simultaneously increase strength and ductility (for grain sizes that are not in the nanoscale regime). However, this result is at odds with the low tensile ductility (9.7%) reported for the smaller grain size of 22 μm (REF.[75]). This is another discrepancy that needs further work to be resolved.

As in FCC HEAs, TRIP effects can be advantageously used in BCC HEAs. The first work[132] to show this effect investigated an off-equiatomic metastable variant of the TiZrHfNbTa alloy, Ti$_{35}$Zr$_{27.5}$Hf$_{27.5}$Nb$_5$Ta$_5$, that was designed using the so-called bond-order, $d$-orbital approach originally developed for Ti alloys. In BCC HEAs, this approach was used to promote a stress-induced transformation from the parent BCC phase to an orthorhombic α″ martensite phase during deformation. The new alloy (referred to as Ti$_{35}$ to distinguish it from the equiatomic alloy Ti$_{20}$) was produced by melting, casting, cold rolling and recrystallization, and had a single-phase BCC structure with a grain size of ~40 μm (REF.[132]). Its yield strength, 540 MPa, was significantly lower than that of the equiatomic alloy produced similarly by cold rolling and recrystallization (958–1,145 MPa for grain sizes of 38–22 μm (REFS[75,131])). However, its elongation to fracture was much higher (~23%[132] versus ~10%[75]). Unlike the equiatomic alloy[75], which shows a monotonic decrease in the work-hardening rate with strain, the work-hardening rate of the Ti$_{35}$ alloy, after an initial decrease, increases sharply at a plastic strain of ~2%. This inflection point corresponds to the start of the BCC–martensite transformation responsible for the TRIP effect. With increasing strain, the amount of martensite increases (saturating at ~65%) and the martensite shows evidence of internal twinning[132]. Together, these TRIP and TWIP phenomena enable the Ti$_{35}$ alloy to undergo extensive work hardening and reach an ultimate tensile strength comparable to that of the equiatomic alloy, but with twice the tensile ductility. Subsequently, a similar TRIP effect in off-equiatomic quaternaries of the Ti–Zr–Hf–Ta system was demonstrated[31].

Although alloy design concepts based on metastability enable substantial gains in strain hardening and ductility through TRIP and TWIP effects, they are effective only at room temperature or modestly elevated temperatures. Thus, for improved creep properties, the use of dispersions of larger amounts of stable, second-phase particles seem to be a more promising design avenue for this alloy family. Also, at elevated temperatures

and in harsh environments, the BCC, refractory-element alloys would require adequate coatings and improved oxidation resistance to survive for long periods of time.

As in some of the FCC HEA systems, in which a beneficial effect of interstitial blending with C was observed, an anomalous interstitial strengthening effect of O was found in the single-phase, equiatomic BCC TiZrHfNb alloy family[133]. Interstitial O remarkably improved the mechanical properties of this alloy at room temperature: the tensile strength increased by 48% and the tensile ductility increased by 95% with 2 at.% oxygen doping of TiZrHfNb. The O forms ordered complexes that simultaneously pin dislocations and promote their cross slip and multiplication.

Finally, similar to the FCC Cantor alloy, the solid-solution state of the BCC TiZrHfNbTa alloy is metastable at intermediate temperatures. Cold rolling followed by annealing at 800 °C resulted in two BCC phases and significant embrittlement relative to the single BCC phase obtained by cold rolling and annealing at 1,000 °C (REF.[75]). Another decomposition was observed when the rolled sheet was annealed for 2 h at 1,200 °C; however, the low volume fraction of the precipitates, which formed both within the grains and on grain boundaries, meant that their nature could not be identified[75]. After severe plastic deformation by high-pressure torsion at room temperature and annealing between 500 °C and 800 °C, decomposition into a Nb-Ta-rich BCC phase and a Zr-Hf-rich HCP phase occurred at lower temperatures, followed by the formation of a Zr-Hf-rich BCC phase at higher temperatures[39]. This decomposition resulted in severe embrittlement[75]. After annealing at 1,000–1,100 °C, a single BCC phase remained, consistent with earlier observations in cold-rolled and annealed material. Similar phase transformations were observed in cast materials[40], indicating that they are thermodynamically stable phases that appear in various processing routes. For high-temperature applications, such transformations and their associated deleterious effects on mechanical properties are a concern and need to be carefully accounted for. For relatively low-temperature applications, metastable microstructures are fine because of slow kinetics (steels and their myriad metastable variants are good examples). Sometimes, metastability may even be desirable, as in the case of TRIP and TWIP alloys. However, for relatively long-term applications at elevated temperatures, one cannot rely on kinetic stabilization; the alloys have to be thermodynamically stable under service conditions.

## Uncharted high-entropy alloys space

If we consider that there are about 60 usable elements in the periodic table, the number of possible new, equi-atomic, five-element HEAs exceeds 5 million; if we contemplate alloys with different numbers of elements, or with non-equiatomic compositions, the number of potential new alloys becomes practically unbounded. The question that immediately arises, then, is how best to interrogate such a vast, uncharted HEA space. There is no simple answer to this question, as any envisioned solution will, by definition, have severe limitations:

the expression 'finding a needle in a haystack' is particularly apt here.

Nevertheless, we consider here three different, nominally high-throughput, screening approaches: one based on purely computational studies, that is, using CALPHAD-type analyses[12,16,17], another using an experimental combinatorial approach[134] and a third, more traditional approach based on mechanistic understanding to adjust the compositions and properties of known alloys[27].

### Broad CALPHAD-type approaches

CALPHAD stands for calculation of phase diagrams, an acronym for thermodynamic models that derive equilibrium-phase diagrams based on analytical Gibbs–Helmholtz free-energy formulations for every phase. The models are cast in polynomial form, referred to as Redlich–Kistler functions, which allows us to readily take first and second derivatives, which are needed to identify, for instance, spinodal phases. The parameters of the polynomials must be fitted using any available and reliable experimental and theoretical data, such as ab initio-derived enthalpies, calorimetry data, metallographic results or statistical models for the entropy. When the free-energy approximations for each of the phases in an alloy system as a function of the relevant state variables — typically, concentration and temperature at constant pressure — are identified, the thermodynamic equilibrium phase for each temperature is calculated by energy minimization using software from, for example, ThermoCalc or CompuTherm. This information is used to trace the phase diagram. It allows the identification of co-existing phases as well as their compositions and volume fractions. This methodology is currently being expanded to alloy systems with a high number of components, targeting particularly the CrMnFeCoNi Cantor system[17]. The Redlich–Kistler functions in these cases also include higher-order interaction parameters, according to the number of components considered. Outside of the fitted ranges and for cases in which unknown competing intermetallic phases appear, this approach currently has limited predictive power.

Therefore, CALPHAD methods can only serve as a first, albeit important, extrapolation step into unchartered compositional territory, as, very often, unexpected intermetallic phases appear. An additional approach might be to also screen compositional regions of interest for competing intermetallic phases that have high energy of formation, a task that is tractable with ab initio methods[49,50].

A problem of the CALPHAD method is that, being based on thermodynamics, it may miss all the metastable, microstructural constituents and transient phases that are at the core of the most successful engineering alloys. Examples are the martensite, bainite, pearlite or Guinier–Preston zones. Quoting from an earlier review[52] "one can envisage that rapid approaches might miss most steels (had they not yet been discovered), due to their polymorphism and tendency to form brittle martensite when cooled quickly".

Moreover, as with the concept of the Materials Genome Initiative[135], an initiative to accelerate the discovery and

deployment of advanced materials, equilibrium approaches alone tell us little about the microstructure, morphology, size, distribution and orientation of the phases present, which control the structure and mechanical properties of the most successful alloys. Indeed, it has consistently been the plague of metallurgists in the development of new structural materials that most theoretical methodologies are not capable of reliably predicting the type and role of microstructures, which are such dominant factors in the control of mechanical properties.

### Combinatorial experimental approaches

Since at least the mid-1960s, combinatorial approaches, which involve high-throughput synthesis and characterization of multiple-alloy compositions, have been used in materials science to rapidly determine phase diagrams in multi-component spaces and screen physical and mechanical properties[136–141]. At least portions of the available compositional space can be surveyed by the fabrication and subsequent characterization of many alloy variants simultaneously[20,21,123,134,142].

Among the different combinatorial methods, four approaches have proven to be particularly useful for HEAs: bulk, rapid alloy prototyping[143]; diffusion couples and diffusion multiples[144,145]; laser and electron additive manufacturing of compositionally graded samples[146]; and combinatorial thin-film materials libraries[147,148].

Rapid alloy prototyping is a combinatorial bulk-processing approach in which secondary specimens can be cut from processed sheets, for example, for uniaxial tensile testing. The method essentially comprises fast, bulk-processing steps, such as slab or strip casting, hot rolling, homogenization, cold rolling and recrystallization. Each casting can, in itself, be compositionally homogeneous or contain chemical gradients along the casting direction, introduced, for instance, by gradually blending a base alloy during an ongoing continuous casting process. This approach has the advantage of providing bulk samples with representative microstructures but is slow compared with thin-film combinatorial methods, which can routinely synthesize multiple, thin-film materials libraries by depositing thin-film composition gradients across a substrate in a single, multi-target sputter experiment. Diffusion multiples, in which specimens with different compositions are brought together at elevated temperatures to produce chemical gradients across their interfaces[144], and compositionally graded additive manufacturing methods[149] are located between rapid alloy prototyping and thin-film methods, and provide access to mesoscopic and millimetre-sized specimens for subsequent property assessment.

Metallographic or XRD characterization of these miniature samples should then be used to yield important information about the phases and microstructures present. For small-scale combinatorial samples, nano-indentation and micro-indentation testing can be used for probing the hardness of the alloys. Disadvantages of small-scale combinatorial methods include limited product size, sometimes too small for a comprehensive screening of functional and/or mechanical properties (such as strain hardening, ductility or fracture toughness), and resulting materials that are too

artificial in terms of microstructure, morphology, size, distribution and orientation of the phases present. Nevertheless, such combinatorial approaches can be valuable in eliminating impractical materials, such as hopelessly brittle alloys, and, thus, can play a key role in reducing the number of alloys to be considered in larger-scale evaluations, such as uniaxial tensile or fracture-toughness tests, which are performed on more realistic product forms.

### Mechanism-based, HEAs design approaches

*Mechanical properties.* An alternative to the systematic compositional screening of new HEAs is a microstructure-based and mechanism-based design approach. Traditional load-carrying materials, such as steels and aluminium alloys, use specific strengthening mechanisms, which depend on temperature, stress and strain rate. Engineering a material's response over a more complex load path requires using not one effect alone but a sequence of mechanisms, including their interplay and associated windows of operation.

Examples of materials treated this way are FeCrNi-based stainless steels or FeMnC-based TWIP steels, two alloy classes with some similarity to FCC HEAs[150]. These materials are strengthened using mechanisms including marked solid-solution and precipitation strengthening, deformation twinning and the formation of ε-martensite and α-martensite phases. The presence of solid solutions in these alloys not only strengthens the matrix but also allows for tuning of the stacking-fault energy, whose magnitude affects the formation of partial dislocations and the occurrence of planar slip and double cross slip. This promotes the formation of rigid dislocation reaction products, enhanced dislocation storage rates, slip patterns and evolving complex dislocation substructures[151]. Reducing the stacking-fault energy promotes the onset of twinning or martensite formation in the desired deformation, stress and strain rate window[152,153]. Nucleation of athermal transformation carriers also depends on the dislocation substructure[154–157]. The key thermodynamic quantity for tuning all these features is the stacking-fault energy, which can, thus, serve as a reliable parameter for alloy design.

In a mechanistic design approach, the sequence of mechanism activation is also important. For optimal strain hardening, dislocations alone are often not sufficient because their multiplication rate eventually saturates and work hardening varies only as the square root of dislocation density. Reducing the stacking-fault energy enables the activation of mechanical twinning when the strain hardening due to dislocations becomes weak. When the additional strain hardening provided by mechanical twinning also gets exhausted, martensite formation can be activated if the stacking-fault energy is sufficiently low ($<20$ mJ.m$^{-2}$)[41,125,158]. Thus, sequential activation of strain-hardening mechanisms can be the pathway for obtaining materials with high formability, all tuned by the same quantity, in this case, the stacking-fault energy[92,159].

Related design ideas based on different key tuning parameters can be gleaned from the treatment of maraging steels: in that case, it is essential to precipitate

intermetallic phases with good matrix coherency, enabling extremely high nucleation rates resulting in nanometre-scale precipitation combined with sufficient antiphase boundary energies for high dislocation-cutting stress. In aluminium alloys, a mechanical response is designed via the transition from early-stage spinodal decomposition to the formation of semi-coherent or incoherent, second-phase particles for exploiting strain hardening by particle cutting or Orowan looping.

These examples show that mechanistic alloy design consists not only of targeting certain sets of deformation mechanisms and their sequential activation but also of identifying and tuning the thermodynamic and structural parameters that govern them. These parameters can be properties such as the stacking-fault energy, lattice coherency or Landau-type spinodal energy landscapes.

One approach to HEA design thus lies in translating and applying these mechanistic design rules to HEAs with the aim of preserving their characteristic advantages, such as massive, solid-solution strengthening, while combining them with the key mechanisms described above (FIG. 4).

A mechanistic approach to the design of HEAs is practicable owing to their high solid-solution content. This means that the design of, for instance, certain spinodal forms, stacking-fault energies or coherent precipitate phases can be achieved by an appropriate choice and quantity of the solid-solution elements that are present anyway in HEAs[27,29].

By taking such a mechanistic perspective, we are, thus, suggesting a targeted development of HEA variants such as TWIP, TRIP, maraging, martensitic or dual-phase HEAs, as well as high-entropy superalloys or spinodally decomposing HEAs. Some of these materials design ideas have already been realized and TWIP[26,27], interstitial[121,122,160], TRIP[161,162] and dual-phase

HEAs[30,161,163] have been obtained, in part also combining different defects depending on the magnitude of the stacking-fault energy[29,124] (FIG. 5).

It should be noted that, in several of these mechanistically designed alloys, some of the original HEA rules were violated; for example, fewer than five alloying elements were used, along with minor alloy ingredients at levels below 5%. Allowing for such compositional deviations from the original HEA rules is justified: first, the mixing entropy curves have a shallow shape so that deviations from equimolar compositions do not alter the configurational entropy substantially; second, compositional tuning of the stacking-fault energy, or other key thermodynamic parameters, is far more important than entropy maximization; third, when striving for mechanical properties, avoiding brittle, intermetallic phases is more of an imperative than obeying static, alloy design rules. The latter point is particularly pertinent as many HEAs with an equimolar composition contain one or more intermetallic phases, which can render them brittle.

*Functional properties.* Although some HEAs have superior mechanical properties, such as high fracture toughness under cryogenic conditions[57] and excellent strength and ductility combinations[25,29,30,53,64] that are consistent with the mechanisms laid out above, only in a few cases will HEAs find their place in the materials selection portfolio based on their mechanical properties, simply because it is hard to surpass established materials such as steels, titanium alloys or nickel-based superalloys in terms of stiffness, strength, ductility, toughness or creep resistance. Thus, the long-term goal of HEA research cannot lie in merely reproducing properties that can already be achieved by well-established, less-expensive competitors.

Accordingly, we believe that the development of future HEAs should also focus on achieving a multifunctional behaviour to marry specific functional properties to the excellent mechanical properties of many of these alloys. As such, the importance of HEAs may well lie in the ability to design unprecedented combinations of mechanical and functional properties in the versatile and seemingly unlimited space of new alloy compositions. In the past, sufficiently ductile and mechanically strong alloys with additional functional features have often enabled application breakthroughs. Traditional examples include steels containing more than 12 wt.% Cr that are strong and corrosion resistant, FeNi invar alloys with negligible thermal expansion in certain temperature ranges, soft, magnetic, FeSi-based alloys with small hysteresis losses, NiTi-based superelastic and shape-memory alloys with good thermomechanical properties and $Nb_3Sn$ type II superconductors with both a high transition temperature and high critical field.

Thus, promising targets for the future development of HEAs include functional properties related to corrosion, hydrogen embrittlement resistance[164,165], stress corrosion resistance, weldability[163], weight reduction, enhanced elastic stiffness or tailored elastic anisotropy, soft and hard magnetic features, combined magnetic and invar response, specific electrical
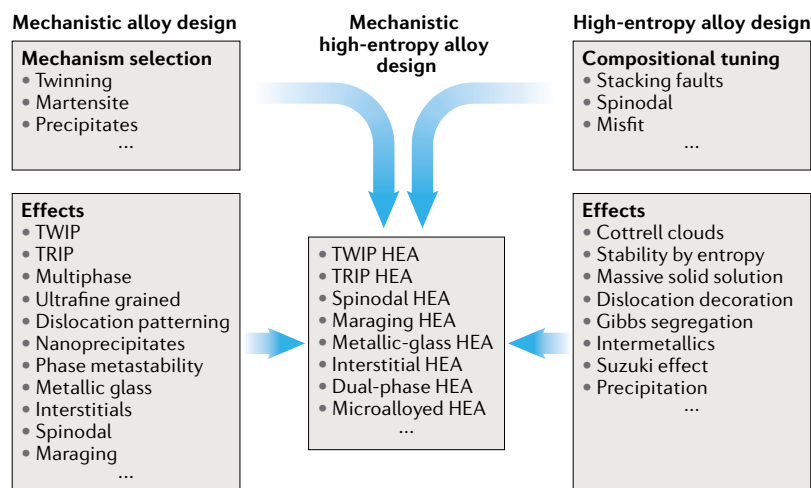


**Mechanistic alloy design**

**Mechanism selection**
- Twinning
- Martensite
- Precipitates
  ...

**Effects**
- TWIP
- TRIP
- Multiphase
- Ultrafine grained
- Dislocation patterning
- Nanoprecipitates
- Phase metastability
- Metallic glass
- Interstitials
- Spinodal
- Maraging
  ...

**Mechanistic high-entropy alloy design**

- TWIP HEA
- TRIP HEA
- Spinodal HEA
- Maraging HEA
- Metallic-glass HEA
- Interstitial HEA
- Dual-phase HEA
- Microalloyed HEA
  ...

**High-entropy alloy design**

**Compositional tuning**
- Stacking faults
- Spinodal
- Misfit
  ...

**Effects**
- Cottrell clouds
- Stability by entropy
- Massive solid solution
- Dislocation decoration
- Gibbs segregation
- Intermetallics
- Suzuki effect
- Precipitation
  ...

Fig. 4 | **A mechanistic approach to the design of high-entropy alloys.** Established effects from conventional alloys such as twinning-induced plasticity (TWIP) or transformation-induced plasticity (TRIP) can be combined with massive solid solution and its associated degrees of freedom for compositional tuning of stacking-fault energy or desired precipitates for the design of several types of new high-entropy alloy (HEA) classes.
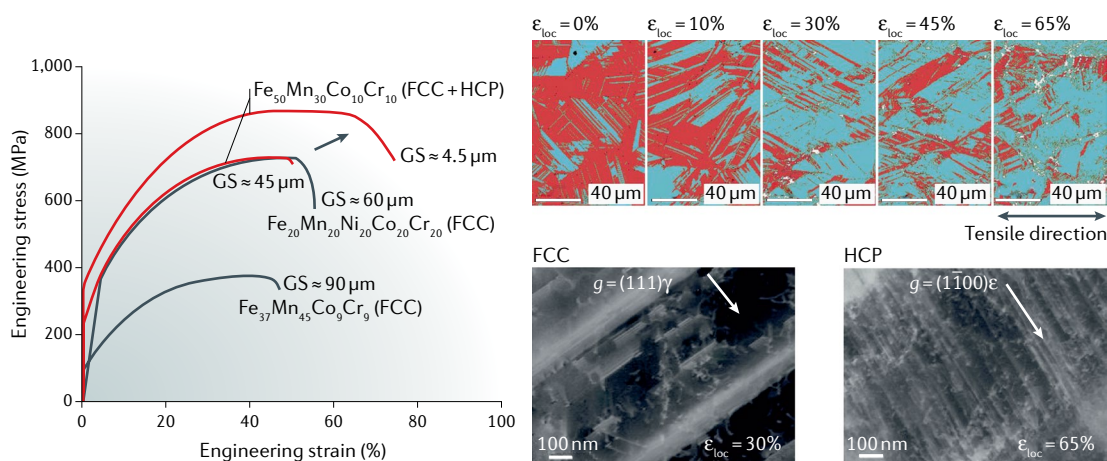
Fig. 5 | **Mechanical properties of the dual-phase, high-entropy, transformation-induced plasticity alloy Fe$_{50}$Mn$_{30}$Co$_{10}$Cr$_{10}$.** Engineering stress–strain curves for the high-entropy alloy Fe$_{50}$Mn$_{30}$Co$_{10}$Cr$_{10}$ (red curves) for two different grain sizes (GS). The associated phase maps for different values of the local strain $\varepsilon_{loc}$ are also shown (red, face-centred cubic, FCC; blue, hexagonal close-packed, HCP; the tensile direction is shown), accompanied by two exemplary dislocation substructures mapped by electron channelling contrast imaging. The phase maps reveal the presence of the two phases before loading and the gradual martensitic transition from FCC to HCP at room temperature during tensile deformation. In the electron channelling contrast images, $g$ is the diffraction vector. The two black curves show the mechanical response of two single-phase, FCC, high-entropy alloys without a transformation-induced plasticity effect and without a HCP phase as reference. At comparable grain size, the dual-phase alloy has both improved strength and ductility, thus breaking the strength–ductility trade-off. Adapted from REF.[122], CC-BY.4.0.

resistivity, magneto-resistivity and electro-migration resistance, shape-memory features, thermoelectric-energy-harvesting capabilities, superconductivity[166,167], surface oxide layers with desired semiconductor features, self-healing or self-reporting bulk or surface behaviour, anti-fouling or antibacterial surfaces oxide layers, biocompatibility, bioresorption and properties relevant for anodic battery materials. These properties are, to a certain extent, available from different materials, but often not in a well-tailored fashion and not combined with excellent mechanical properties at extreme temperatures and environmental conditions, low price and good processing behaviour.

HEAs may open additional pathways for blue-sky research, specifically for less mechanistically driven studies that are open to unexpected property discoveries. The design and use of quantum mechanically guided HEA treasure maps that point towards promising compositions for functionally oriented structure–property relationships will be helpful in this regard.

In the past few years, papers on materials that might be broadly classified as 'high-entropy ceramics' with the potential for interesting functional properties have begun to appear. Examples include oxides[168–174], carbides[175–180], nitrides[181] and diborides[182,183].

## Prospects and future opportunities

HEAs have taken the field of materials science, or, more precisely, metallurgy, by storm; indeed, they are likely to be central to the field of structural, and perhaps functional, materials for another decade or longer. As we discussed, the high-entropy phenomenon has been principally driven by three main factors: the exceptional mechanical properties of a few specific alloys, most notably the FCC CrCoNi-based alloys, especially

for cryogenic temperature applications; the search for new refractory HEAs that can operate with sustained strength at ever-increasing temperatures, a difficult pursuit because of the limited ductility and oxidation resistance of these materials; and the prospect of discovering new materials with unprecedented properties, or combinations of properties, from the seemingly unbounded list of possible multiple-principal-element materials, although this is a non-trivial exercise in light of the methods currently available to venture into uncharted materials, composition and microstructural space. At present, the field has been dominated by the first factor, as the Cantor alloy and its derivatives have displayed truly compelling mechanical properties, coupled with now several successful attempts at microstructural optimization and new mechanistic interpretations to underpin their impressive mechanical performance. However, we suspect that the latter two factors will ultimately come to the fore as the quest for higher-temperature structural materials remains a focus in materials science, which is driven by advances in aerospace and now hypersonic activities; the possible discovery of new, hitherto unknown supermaterials will forever be a worthy cause.

However, in the short term, several specific issues remain to be resolved pertaining to what may make HEAs distinct from conventional alloys. One is the role of local chemical order on the macroscopic properties of HEAs. DFT-based Monte Carlo simulations on equimolar CrCoMo with several hundred atoms[88] and molecular dynamics simulations with a few million atoms using a newly developed classical potential for CrCoMo (REF.[184]) both predict that the degree of local chemical order in CrCoNi has a marked influence on its stacking-fault energy (FIG. 6), twinning energy, energy
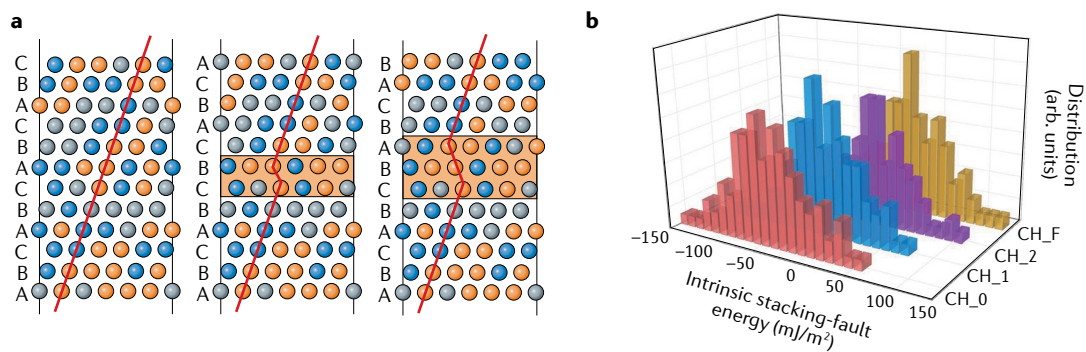
Fig. 6 | **Role of local chemical ordering on the stacking-fault energy calculated by density functional theory for solid-solution CrCoNi alloys. a |** Side view of atomic configurations in an originally face-centred cubic structure (left), with intrinsic stacking faults (middle) and extrinsic stacking faults (right). The orange shade indicates the stacking fault; the plane labels A, B and C represent close-packed (111) planes. **b |** Distribution of the intrinsic stacking-fault energy, $\gamma_{isf}$, for CrCoNi alloys in four specific states (CH_0, CH_1, CH_2 and CH_F) spanning from random solid solutions to the highest degree of chemical ordering. In total, 108 stacking faults were considered for analysis in each state. These figures indicate that the presence of local chemical ordering in high-entropy alloys can have a profound effect on parameters such as the stacking-fault energy (and related parameters such as the energy for twinning), which are known to have a marked influence on plastic deformation and, hence, on the generation of both strength and ductility. Adapted from REF.[88].

difference between the FCC and HCP phases (which governs the TRIP and TWIP effects) and formation energy for point defects, all of which are parameters that are known to markedly affect the strength and deformation of CrCoNi-based HEAs. However, the role of local chemical order in HEAs remains an open issue because it has yet to be convincingly confirmed experimentally. Only one study[185], using extended X-ray adsorption fine structure on CrCoNi, has suggested that Cr atoms display a preference to bonding to Ni and Co atoms, rather than other Cr atoms, which is consistent with the DFT-based Monte Carlo predictions. However, the fascinating notion of tuning atomic order to achieve enhanced macroscale mechanical properties awaits more convincing experimental confirmation that such local chemical order actually exists in apparently random HEA solid solutions.

Further opportunities lie in the exploration of thermodynamics, microstructure evolution and properties of HEAs with near-zero stacking-fault energies. Metastable HEAs with small stacking-fault energy and deformation-driven twinning and martensite formation have been studied; yet, even more complex substructures have been recently reported for dual-phase, FCC–HCP HEAs with near-zero or slightly negative stacking-fault energy. In these materials, the matrix can assume both the HCP and the FCC structure, owing to the energetic equivalence of the co-existing phases[124,186]. The deformation-driven nanoscale refinement observed in such alloys seems to be further promoted by the very small coherent interface energies among the different phases and microstructure ingredients, that is, the FCC phase, the HCP phase, twins and stacking faults. The similarity in phase energy can also lead to a bidirectional TRIP effect, in which FCC-structured matrix portions transform under load into HCP regions and vice versa, depending on the local, micromechanical stresses. This effect leads to an extreme microstructure refinement down to the nanometre regime[124].

Interesting effects in HEAs may be expected owing to the multi-element co-decoration of lattice defects. Whereas traditional segregation phenomena such as Cottrell atmospheres, grain-boundary segregation and Suzuki decoration are well known, they may work differently when involving many interacting species that co-segregate. The thermodynamic and kinetic competition among the decorating species, as well as their interactions once segregated, may lead to novel structures and phenomena.

Another avenue of interesting research pertains to the role of interstitial elements in HEAs. Several groups studied the influence of C on phase stability, carbide formation and mechanical properties, but other elements such as N, O, H and B are also interesting doping candidates in HEAs. For example, it was recently shown that O, which is normally a rather harmful interstitial element in metals, aids in forming ordered O-Ti-Zr-rich clusters in an O-doped TiZrHfNb HEA, enhancing its strength and ductility[133]. Even the most harmful interstitial element in metallic alloys, H, has been found to lend a certain resistance to hydrogen embrittlement in HEAs. This effect was attributed to the fact that H reduces the material's stacking-fault energy, thus providing higher local strain hardening[165]. To aid future research efforts, several theoretical and experimental tools need to be improved (BOX 3).

In general, we believe that more attention should be placed on potential innovative applications for HEAs. Most efforts in the field are focused on mechanical properties but recent works also revealed unexpected features of HEAs that might be interesting for magnetic, invar or catalytic applications. Particularly, HEAs with multi-functional properties might lead to new processes or products. Thus, it will be worth exploring where specific properties may be expected that are better than those of established material classes, such as steels or aluminium alloys.

In this regard, it is pertinent to note that nature effectively designs structural architectures to create

Box 3 | **Tools needed to further advance the field**

*Improved computational and machine learning tools for predicting multi-component phase diagrams and transport coefficients*. Special emphasis should be placed on the roles of interstitial elements such as B known for their beneficial effects on interface cohesion in conventional alloys, on reaching higher precision in the prediction of phase transformations and on low-temperature equilibrium and non-equilibrium phases and microstructure states, because some high-entropy alloys (HEAs) target cryogenic applications.

*Improved experimental and theoretical tools to study short-range ordering effects*. Local chemical order appears to play an important role in HEAs, although it is still relatively unexplored. With respect to theoretical tools, density functional theory methods have been used to examine local order in HEAs (FIG. 6) but can only look at a limited number of atoms (a few hundred). Molecular dynamics techniques are less accurate but can consider far more atoms (on the order of millions). However, a serious limitation is the number of available potentials and there is a pressing need to develop accurate atomic potentials for the combinations of three to five elemental atoms. With respect to experimental methods, improvements are needed in correlative, high-precision probing of the local chemical composition of solids, both in precipitates and matrix phases, and at lattice defects. High-resolution analytical electron microscopy does not yield true atomically resolved chemistry but, rather, integrated atomic column compositions, yet with excellent structure resolution. With these reservations, 4D scanning transmission electron microscopy techniques, which use series of 2D diffraction patterns collected at several nanometre-scale locations using direct electron detectors operating at a frame rate of thousands of frames per second, perhaps offer the most promise. Atom probe tomography provides near-atomic-scale chemical resolution with very high precision but can suffer from aberration deficiencies, lack of structural resolution and overlap in the peaks detected because different ions can have the same mass-to-charge ratio. Field ion microscopy provides the highest single, atomic positioning fidelity but lacks quantitative chemical sensitivity. All of these atom-resolving characterization tools thus face challenges when it comes to the high-resolution analysis of HEAs and require improvement of several features, including detectors and methods layout and simulation-enhanced and machine-learning-enhanced image analysis techniques. Another important goal will be to integrate information gained from high-resolution imaging at the atomic scale into descriptions of material behaviour at larger scales, at which features such as dislocations, twins and grain boundaries, which determine many mechanical properties, are observed.

*Development of cost-effective HEAs*. Cost factors and sustainability should also be taken into account in the development (or, rather, maturation) of HEAs. Such considerations include not only the price of alloying elements but also the feasibility of scrap recovery and recycling. The materials' lifetime and sustainability (such as enhanced longevity and high damage tolerance under harsh conditions) can be tackled in material-specific life cycle assessments.

*High-throughput experimental assessment*. Another area that needs improvement is that of high-throughput material synthesis and processing methods. The development of more efficient experimental screening tools, especially for structure-sensitive properties, remains a challenge.

multi-functional materials with unusual combinations of properties that are often difficult to achieve in a single, synthetic material; for example, seashells possess both strength and ductility, which are often mutually exclusive properties in man-made materials[187]. HEAs offer the possibility of multi-functionality but without the need for bottom-up (atomic-scale) processing. For example, strain hardening to attain strength and ductility in CrCoNi-based HEAs is promoted not simply through structure but also via composition and the associated mechanism tuning. HEAs with excellent mechanical properties remain to be engineered to achieve other properties, such as corrosion and/or oxidation resistance or resistance to stress-corrosion

cracking, for example by alloy additions to change the composition of the protective self-passivating oxides that form on their surface. Understanding and quantifying diffusion in multi-component systems is another area of research that needs to be revived to develop creep-resistant HEAs.

These challenges will undoubtedly provide innumerable promising pursuits for materials scientists and engineers in the never-ending mission to design and develop superior materials to meet the needs of next-generation engineering applications, particularly for energy and transportation.

Published online 18 June 2019

1. Yeh, J. W. et al. Nanostructured high-entropy alloys with multiple principal elements: novel alloy design concepts and outcomes. *Adv. Eng. Mater.* **6**, 299–303 (2004).
2. Cantor, B., Chang, I. T. H., Knight, P. & Vincent, A. J. B. Microstructural development in equiatomic multicomponent alloys. *Mater. Sci. Eng. A* **375**, 213–218 (2004).
3. Cantor, B. Multicomponent and high entropy alloys. *Entropy* **16**, 4749–4768 (2014).
4. Miracle, D. B. & Senkov, O. N. A critical review of high entropy alloys and related concepts. *Acta Mater.* **122**, 448–511 (2017).
5. Huang, P. K., Yeh, J. W., Shun, T. T. & Chen, S. K. Multi-principal-element alloys with improved oxidation and wear resistance for thermal spray coating. *Adv. Eng. Mater.* **6**, 74–78 (2004).
6. Tong, C. J. et al. Microstructure characterization of AlxCoCrCuFeNi high-entropy alloy system with multi-principal elements. Metall. *Mater. Trans. A Phys. Metall. Mater. Sci.* **36**, 881–893 (2005).
7. Zhou, Y. J., Zhang, Y., Wang, Y. L. & Chen, G. L. Solid solution alloys of AlCoCrFeNiTix with excellent room-temperature mechanical properties. *Appl. Phys. Lett.* **90**, 181904 (2007).
8. Wang, F. J. & Zhang, Y. Effect of Co addition on crystal structure and mechanical properties of Ti0.5CrFeNiAlCo high entropy alloy. *Mater. Sci. Eng. A* **496**, 214–216 (2008).
9. Shun, T. T., Hung, C. H. & Lee, C. F. Formation of ordered/disordered nanoparticles in FCC high entropy alloys. *J. Alloys. Compd.* **493**, 105–109 (2010).
10. Singh, S., Wanderka, N., Murty, B. S., Glatzel, U. & Banhart, J. Decomposition in multi-component AlCoCrCuFeNi high-entropy alloy. *Acta Mater.* **59**, 182–190 (2011).
11. Yardley, V. & Povstugar, V. et al. On local phase equilibria and appearance of nanoparticles in the microstructure of single-crystal Ni-base superalloys. *Adv. Eng. Mater.* **18**, 1556–1567 (2016).
12. Zhang, C., Zhang, F., Chen, S. & Cao, W. Computational thermodynamics aided high-entropy alloy design. *JOM* **64**, 839–845 (2012).
13. Zhang, F. et al. An understanding of high entropy alloys from phase diagram calculations. *CALPHAD* **45**, 1–10 (2014).
14. Gao, M. C. et al. Thermodynamics of concentrated solid solution alloys. *Curr. Opin. Sol. State Mater. Sci.* **21**, 238–251 (2017).
15. Mao, H. H., Chen, H. L. & Chen, Q. TCHEA1: a thermodynamic database not limited for

"high entropy" alloys. *J. Phase Equilibria Diffus.* **38**, 353–368 (2017).

16. Gorsse, S. & Tancret, F. Current and emerging practices of CALPHAD toward the development of high entropy alloys and complex concentrated alloys. *J. Mater. Res.* **33**, 2899–2923 (2018).

17. Gorsse, S. & Senkov, O. N. About the reliability of CALPHAD predictions in multicomponent systems. *Entropy* **20**, 899 (2018).

18. Abu-Odeh, A. et al. Efficient exploration of the high entropy alloy composition-phase space. *Acta Mater.* **152**, 41–57 (2018).

19. Chen, H. L., Mao, H. H. & Chen, Q. Database development and CALPHAD calculations for high entropy alloys: challenges, strategies, and tips. *Mater. Chem. Phys.* **210**, 279–290 (2018).

20. Borkar, T. et al. A combinatorial assessment of Al*x*CrCuFeNi2 (0 < x < 1.5) complex concentrated alloys: microstructure, microhardness, and magnetic properties. *Acta Mater.* **116**, 63–76 (2016).

21. Borkar, T. & Chaudhary, V. et al. A combinatorial approach for assessing the magnetic properties of high entropy alloys: role of Cr in AlCo*x*Cr1-*x*FeNi. *Adv. Eng. Mater.* **19**, 1700048 (2017).

22. Kauffmann, A. et al. Combinatorial exploration of the high entropy alloy system Co-Cr-Fe-Mn-Ni. *Surf. Coat. Technol.* **325**, 174–180 (2017).

23. Li, Y. J., Kostka, A., Savan, A., Stein, H. S. & Ludwig, A. Accelerated atomic-scale exploration of phase evolution in compositionally complex materials. *Mater. Horizons.* **5**, 86–92 (2018).

24. Li, Y. J., Kostka, A., Savan, A. & Ludwig, A. Atomic-scale investigation of fast oxidation kinetics of nanocrystalline CrMnFeCoNi alloy thin films. *J. Alloys. Compd.* **766**, 1080–1085 (2018).

25. Otto, F. et al. The influences of temperature and microstructure on the tensile properties of a CoCrFeMnNi high-entropy alloy. *Acta Mater.* **61**, 5743–5755 (2013).

26. Deng, Y. et al. Design of a twinning-induced plasticity high entropy alloy. *Acta Mater.* **94**, 124–133 (2015).

27. Li, Z. & Raabe, D. Strong and ductile non-equiatomic high-entropy alloys: design, processing, microstructure, and mechanical properties. *JOM* **69**, 2099–2106 (2017).

28. Jo, Y. H. et al. Cryogenic strength improvement by utilizing room-temperature deformation twinning in a partially recrystallized VCrMnFeCoNi high-entropy alloy. *Nat. Commun.* **8**, 15719 (2017).

29. Li, Z., Pradeep, K. G., Deng, Y., Raabe, D. & Tasan, C. C. Metastable high-entropy dual-phase alloys overcome the strength-ductility trade-off. *Nature* **534**, 227–230 (2016).

30. Li, Z., Körmann, F., Grabowski, B., Neugebauer, J. & Raabe, D. Ab initio assisted design of quinary dual-phase high-entropy alloys with transformation-induced plasticity. *Acta Mater.* **136**, 262–270 (2017).

31. Huang, H. L. et al. Phase-transformation ductilization of brittle high-entropy alloys via metastability engineering. *Adv. Mater.* **29**, 1701678 (2017).

32. Otto, F., Yang, Y., Bei, H. & George, E. P. Relative effects of enthalpy and entropy on the phase stability of equiatomic high-entropy alloys. *Acta Mater.* **61**, 2628–2638 (2013).

33. Poletti, M. G. & Battezzati, L. Electronic and thermodynamic criteria for the occurrence of high-entropy alloys in metallics systems. *Acta Mater.* **75**, 297–306 (2014).

34. Ma, D., Grabowski, B., Körmann, F., Neugebauer, J. & Raabe, D. Ab initio thermodynamics of the CoCrFeMnNi high entropy alloy: importance of entropy contributions beyond the configurational one. *Acta Mater.* **100**, 90–97 (2015).

35. Schön, C. G., Duong, T., Wang, Y. & Arróyave, R. Probing the phase stability in highly concentrated alloys. *Acta Mater.* **148**, 263–279 (2018).

36. Schuh, B. et al. Mechanical properties, microstructure and thermal stability of a nanocrystalline CoCrFeMnNi high-entropy alloy after severe plastic deformation. *Acta Mater.* **96**, 258–268 (2015).

37. Pickering, E. J., Munoz-Moreno, R., Stone, H. J. & Jones, N. G. Precipitation in the equiatomic high-entropy alloy CrMnFeCoNi. *Scr. Mater.* **113**, 106–109 (2016).

38. Otto, F. et al. Decomposition of the single-phase high-entropy alloy CrMnFeCoNi after prolonged anneals at intermediate temperatures. *Acta Mater.* **112**, 40–52 (2016).

39. Schuh, B. et al. Thermodynamic instability of a nanocrystalline, single-phase TiZrNbHfTa alloy and its impact on the mechanical properties. *Acta Mater.* **142**, 201–212 (2018).

40. Stepanov, N. D., Yurchenko, N. Yu., Zherebtsov, S. V., Tikhonovsky, M. A. & Salishchev, G. A. Aging behavior of the HfNbTaTiZr high entropy alloy. *Mater. Lett.* **211**, 87–90 (2018).

41. Ma, D. et al. Phase stability of non-equiatomic CoCrFeMnNi high entropy alloys. *Acta Mater.* **98**, 288–296 (2015).

42. Tian, F. et al. Structural stability of NiCoFeCrAl high-entropy alloy from ab initio theory. *Phys. Rev. B* **88**, 085128 (2013).

43. van de Walle, A. & Asta, M. Self-driven lattice-model Monte Carlo simulations of alloy thermodynamic properties and phase diagrams. Model. *Simul. Mat. Sci. Eng.* **10**, 521–538 (2002).

44. Senkov, O. N., Miller, J. D., Miracle, D. B. & Woodward, C. Accelerated exploration of multi-principal element alloys for structural applications. *CALPHAD* **50**, 32–48 (2015).

45. Senkov, O. N. et al. CALPHAD-aided development of quaternary multi-principal element refractory alloys based on NbTiZr. *J. Alloys. Compd.* **783**, 729–742 (2019).

46. Yeh, J. W. Alloy design strategies and future trends in high-entropy alloys. *JOM* **65**, 1759–1771 (2013).

47. Tsai, M. H. & Yeh, J. W. High-entropy alloys: a critical review. *Mater. Res. Lett.* **2**, 107–123 (2014).

48. Zhang, Y. et al. Microstructures and properties of high-entropy alloys. *Prog. Mater. Sci.* **61**, 1–93 (2014).

49. Troparevsky, M. C., Morris, J. R., Kent, P. R. C., Lupini, A. R. & Stocks, G. M. Criteria for predicting the formation of single-phase high-entropy alloys. *Phys. Rev. X* **5**, 011041 (2015).

50. Troparevsky, M. C. et al. Beyond atomic sizes and Hume-Rothery rules: understanding and predicting high-entropy alloys. *JOM* **67**, 2350–2363 (2015).

51. King, D. J. M., Middleburgh, S. C., McGregor, A. G. & Cortie, M. B. Predicting the formation and stability of single phase high-entropy alloys. *Acta Mater.* **104**, 172–179 (2016).

52. Pickering, E. J. & Jones, N. G. High-entropy alloys: a critical assessment of their founding principles and future prospects. *Int. Mater. Rev.* **61**, 183–202 (2016).

53. Gali, A. & George, E. P. Tensile properties of high- and medium-entropy alloys. *Intermetallics* **39**, 74–78 (2013).

54. Tsai, K. Y., Tsai, M. H. & Yeh, J. W. Sluggish diffusion in Co–Cr–Fe–Mn–Ni high-entropy alloys. *Acta Mater.* **61**, 4887–4897 (2013).

55. Liu, W. H., Wu, Y., He, J. Y., Nieh, T. G. & Lu, Z. P. Grain growth and the Hall-Petch relationship in a high-entropy FeCrNiCoMn alloy. *Scr. Mater.* **68**, 526–529 (2013).

56. He, J. Y. et al. Steady state flow of the FeCoNiCrMn high entropy alloy at elevated temperatures. *Intermetallics* **55**, 9–14 (2014).

57. Gludovatz, B. et al. A fracture-resistant high-entropy alloy for cryogenic applications. *Science* **345**, 1153–1158 (2014).

58. Otto, F., Hanold, N. L. & George, E. P. Microstructural evolution after thermomechanical processing in an equiatomic single-phase CoCrFeMnNi high-entropy alloy with special focus on twin boundaries. *Intermetallics* **54**, 39–48 (2014).

59. Wu, Z., Bei, H., Pharr, G. M. & George, E. P. Temperature dependence of the mechanical properties of equiatomic solid solution alloys with face-centered cubic crystal structures. *Acta Mater.* **81**, 428–441 (2014).

60. Haglund, A., Koehler, M., Catoor, D., George, E. P. & Keppens, V. Polycrystalline elastic moduli of a high-entropy alloy at cryogenic temperatures. *Intermetallics* **58**, 62–64 (2015).

61. Laplanche, G. et al. Temperature dependencies of the elastic moduli and thermal expansion coefficient of an equiatomic, single-phase CoCrFeMnNi high-entropy alloy. *J. Alloys. Compd.* **623**, 348–353 (2015).

62. Laurent-Brocq, M. et al. Insights into the phase diagram of the CrMnFeCoNi high entropy alloy. *Acta Mater.* **88**, 355–365 (2015).

63. Laplanche, G., Horst, O., Otto, F., Eggeler, G. & George, E. P. Microstructural evolution of a CoCrFeMnNi high-entropy alloy after swaging and annealing. *J. Alloys. Compd.* **647**, 548–557 (2015).

64. Laplanche, G., Kostka, A., Horst, O. M., Eggeler, G. & George, E. P. Microstructure evolution and critical stress for twinning in the CrMnFeCoNi high-entropy alloy. *Acta Mater.* **118**, 152–163 (2016).

65. Bracq, G. et al. The fcc solid solution stability in the Co-Cr-Fe-Mn-Ni multi-component system. *Acta Mater.* **128**, 327–336 (2017).

66. Laplanche, G., Bonneville, J., Varvenne, C., Curtin, W. A. & George, E. P. Thermal activation parameters of plastic flow reveal deformation mechanisms in the CrMnFeCoNi high-entropy alloy. *Acta Mater.* **143**, 257–264 (2018).

67. Laplanche, G. et al. Phase stability and kinetics of σ-phase precipitation in CrMnFeCoNi high-entropy alloys. *Acta Mater.* **161**, 338–351 (2018).

68. Haas, S. et al. Entropy determination of single-phase high entropy alloys with different crystal structures over a wide temperature range. *Entropy* **20**, 654 (2018).

69. Senkov, O. N., Wilks, G. B., Miracle, D. B., Chuang, C. P. & Liaw, P. K. Refractory high-entropy alloys. *Intermetallics* **18**, 1758–1765 (2010).

70. Senkov, O. N. & Woodward, C. F. Microstructure and properties of a refractory NbCrMo0.5Ta0.5TiZr alloy. *Mater. Sci. Eng. A* **529**, 311–320 (2011).

71. Senkov, O. N., Wilks, G. B., Scott, J. M. & Miracle, D. B. Mechanical properties of Nb25Mo25Ta25W25 and V20Nb20Mo20Ta20W20 refractory high entropy alloys. *Intermetallics* **19**, 698–706 (2011).

72. Senkov, O. N., Scott, J. M., Senkova, S. V., Miracle, D. B. & Woodward, C. F. Microstructure and room temperature properties of a high-entropy TaNbHfZrTi alloy. *J. Alloys. Compd.* **509**, 6043–6048 (2011).

73. Senkov, O. N. et al. Microstructure and elevated temperature properties of a refractory TaNbHfZrTi alloy. *J. Mater. Sci.* **47**, 4062–4074 (2012).

74. Senkov, O. N., Senkova, S. V. & Woodward, C. Effect of aluminum on the microstructure and properties of two refractory high-entropy alloys. *Acta Mater.* **68**, 214–228 (2014).

75. Senkov, O. N. & Semiatin, S. L. Microstructure and properties of a refractory high-entropy alloy after cold working. *J. Alloys. Compd.* **649**, 1110–1123 (2015).

76. Juan, C. C. et al. Enhanced mechanical properties of HfMoTaTiZr and HfMoNbTaTiZr refractory high-entropy alloys. *Intermetallics* **62**, 76–83 (2015).

77. Couziné, J. P. et al. On the room temperature deformation mechanisms of a TiZrHfNbTa refractory high-entropy alloy. *Mater. Sci. Eng. A* **645**, 255–263 (2015).

78. Sheikh, S. et al. Alloy design for intrinsically ductile refractory high-entropy alloys. *J. Appl. Phys.* **120**, 164902 (2016).

79. Takeuchi, A., Amiya, K., Wada, T., Yubuta, K. & Zhang, W. High-entropy alloys with a hexagonal close-packed structure designed by equi-atomic alloy strategy and binary phase diagrams. *JOM* **66**, 1984–1992 (2014).

80. Feuerbacher, M., Heidelmann, M. & Thomas, C. Hexagonal high-entropy alloys. *Mater. Res. Lett.* **3**, 1–6 (2015).

81. Zhao, Y. J. et al. A hexagonal close-packed high-entropy alloy: the effect of entropy. *Mater. Des.* **96**, 10–15 (2016).

82. Soler, R. et al. Microstructural and mechanical characterization of an equiatomic YGdTbDyHo high entropy alloy with hexagonal close-packed structure. *Acta Mater.* **156**, 86–96 (2018).

83. Qiao, J. W. et al. Rare-earth high entropy alloys with hexagonal close-packed structure. *J. Appl. Phys.* **124**, 195101 (2018).

84. Lilensten, L. et al. New structure in refractory high-entropy alloys. *Mater. Lett.* **132**, 123–125 (2014).

85. Bhattacharjee, P. P. et al. Microstructure and texture evolution during annealing of equiatomic CoCrFeMnNi high-entropy alloy. *J. Alloys. Compd.* **587**, 544–552 (2014).

86. Salishchev, G. A. et al. Effect of Mn and V on structure and mechanical properties of high-entropy alloys based on CoCrFeNi system. *J. Alloys. Compd.* **591**, 11–21 (2014).

87. Stepanov, N. D. et al. High temperature deformation behavior and dynamic recrystallization in CoCrFeMnNi high entropy alloy. *Mater. Sci. Eng. A* **636**, 188–195 (2015).

88. Ding, J., Yu, Q., Asta, M. & Ritchie, R. O. Tunable stacking fault energies by tailoring local chemical order in CrCoNi medium-entropy alloys. *Proc. Natl. Acad. Sci. USA* **115**, 8819–8924 (2018).

89. Tracy, C. L. et al. High pressure synthesis of a hexagonal close-packed phase of the high-entropy alloy CrMnFeCoNi. *Nat. Commun.* **8**, 15634 (2017).

90. Zhang, F. et al. Polymorphism in a high-entropy alloy. *Nat. Commun.* **8**, 15687 (2017).

91. Okamoto, N. L. et al. Size effect, critical resolved shear stress, stacking fault energy, and solid solution strengthening in the CrMnFeCoNi high-entropy alloy. *Sci. Rep.* **6**, 35863 (2016).

92. Zaddach, A. J., Niu, C., Koch, C. C. & Irving, D. L. Mechanical properties and stacking fault energies of NiFeCrCoMn high-entropy alloy. *JOM* **65**, 1780–1789 (2013).

93. Smith, T. M. et al. Atomic-scale characterization and modeling of 60° dislocations in a high-entropy alloy. *Acta Mater.* **110**, 352–362 (2016).

94. Zhang, Z. J. et al. Nanoscale origins of the damage tolerance of the high-entropy alloy CrMnFeCoNi. *Nat. Commun.* **6**, 10143 (2015).

95. Meyers, M. A., Vöhringer, O. & Lubarda, V. A. The onset of twinning in metals: a constitutive description. *Acta Mater.* **49**, 4025–4039 (2001).

96. Abuzaid, W. & Sehitoglu, H. Critical resolved shear stress for slip and twin nucleation in single crystalline FeNiCoCrMn high entropy alloy. *Mater. Char.* **129**, 288–299 (2017).

97. Kireeva, I. V., Chumlyakov, Yu. I., Pobedennaya, Z. V., Kuksgausen, I. V. & Karaman, I. Orientation dependence of twinning in single crystalline CoCrFeMnNi high-entropy alloy. *Mater. Sci. Eng. A* **707**, 176–181 (2017).

98. Wu, Y., Bönisch, M., Alkan, S., Abuzaid, W. & Sehitoglu, H. Experimental determination of latent hardening coefficients in FeMnNiCoCr. *Int. J. Plastic.* **105**, 239–260 (2018).

99. Kireeva, I. V., Chumlyakov, Yu. I., Pobedennaya, Z. V., Vyrodova, A. V. & Karaman, I. Twinning in [001]-oriented single crystals of CoCrFeMnNi high-entropy alloy at tensile deformation. *Mater. Sci. Eng. A* **713**, 253–259 (2018).

100. Bönisch, M., Wu, Y. & Sehitoglu, H. Hardening by slip-twin and twin-twin interactions in FeMnNiCoCr. *Acta Mater.* **153**, 391–403 (2018).

101. Stepanov, N. et al. Effect of cryo-deformation on structure and properties of CoCrFeNiMn high-entropy alloy. *Intermetallics* **59**, 8–17 (2015).

102. Patriarca, L., Ojha, A., Sehitoglu, H. & Chumlyakov, Y. I. Slip nucleation in single crystal FeNiCoCrMn high entropy alloy. *Scr. Mater.* **112**, 54–57 (2016).

103. Koppenaal, T. J. & Fine, M. E. Solid solution strengthening in alpha Cu-Al single crystals. *Trans. Metall. Soc. AIME* **224**, 347–353 (1962).

104. Basinski, Z. S., Foxall, R. A. & Pascual, R. Stress equivalence of solution hardening. *Scr. Metall.* **6**, 807–814 (1972).

105. Traub, H., Neuhäuser, H. & Schwink, Ch. Investigation of yield region of concentrated Cu-Ge and Cu-Zn single crystals. 1. Critical resolved shear-stress, slip line formation and true strain rate. *Acta Metall.* **25**, 437–446 (1977).

106. Butt, M. Z. & Feltham, P. Solid-solution hardening. *Acta Metall.* **26**, 167–173 (1978).

107. Wille, Th. & Schwink, Ch. Precision measurements of critical resolved shear-stress in CuMn alloys. *Acta Metall.* **34**, 1059–1069 (1986).

108. Wille, Th, Gieseke, W. & Schwink, Ch Quantitative analysis of solution hardening in selected copper alloys. *Acta Metall.* **35**, 2679–2693 (1987).

109. Varvenne, C., Aitor, L. & Curtin, W. A. Theory of strengthening in fcc high entropy alloys. *Acta Mater.* **118**, 164–176 (2016).

110. Varvenne, C., Leyson, G. P. M., Ghazisaeidi, M. & Curtin, W. A. Solute strengthening in random alloys. *Acta Mater.* **124**, 660–683 (2017).

111. Haasen, P. Plastic deformation of nickel single crystals at low temperatures. *Philos. Mag.* **3**, 384–418 (1958).

112. Okamoto, N. L., Yuge, K., Tanaka, K., Inui, H. & George, E. P. Atomic displacement in the CrMnFeCoNi high-entropy alloy − a scaling factor to predict solid solution strengthening. *AIP Adv.* **6**, 125008 (2016).

113. Zhang, Z. J. et al. Dislocation mechanisms and 3D twin architectures generate exceptional strength-ductility-toughness combination in CrCoNi medium-entropy alloy. *Nat. Commun.* **8**, 14390 (2017).

114. Zhao, Y. L. et al. Heterogeneous precipitation behavior and stacking-fault-mediated deformation in a CoCrNi-based medium-entropy alloy. *Acta Mater.* **138**, 72–82 (2017).

115. Sohn, S. S. et al. Ultrastrong medium-entropy single-phase alloys designed via severe lattice distortion. *Adv. Mater.* **31**, 1807142 (2019).

116. Gludovatz, B. et al. Exceptional damage-tolerance of a medium-entropy alloy CrCoNi at cryogenic temperatures. *Nat. Commun.* **7**, 10602 (2016).

117. Laplanche, G. et al. Reasons for the superior mechanical properties of medium-entropy CrCoNi compared to high-entropy CrMnFeCoNi. *Acta Mater.* **128**, 292–303 (2017).

118. Yang, M. et al. Dynamically reinforced heterogeneous grain structure prolongs ductility in a medium-entropy alloy with gigapascal yield strength. *Proc. Natl. Acad. Sci. USA* **115**, 7224–7229 (2018).

119. Slone, C. E., Miao, J., George, E. P. & Mills, M. J. Achieving ultra-high strength and ductility in equiatomic CrCoNi with partially recrystallized microstructures. *Acta Mater.* **165**, 497–507 (2019).

120. Tasan, C. C. et al. Composition dependence of phase stability, deformation mechanisms, and mechanical properties of the CoCrFeMnNi high-entropy alloy system. *JOM* **66**, 1993–2001 (2014).

121. Wang, M., Li, Z. & Raabe, D. In-situ SEM observation of phase transformation and twinning mechanisms in an interstitial high-entropy alloy. *Acta Mater.* **147**, 236–246 (2018).

122. Li, Z., Tasan, C. C., Springer, H., Gault, B. & Raabe, D. Interstitial atoms enable joint twinning and transformation induced plasticity in strong and ductile high-entropy alloys. *Sci. Rep.* **7**, 40704 (2017).

123. Pradeep, K. G. et al. Non-equiatomic high entropy alloys: approach towards rapid alloy screening and property-oriented design. *Mater. Sci. Eng. A* **648**, 183–192 (2015).

124. Lu, W., Liebscher, C. H., Dehm, G., Raabe, D. & Li, Z. Bidirectional transformation enables hierarchical nanolaminate dual-phase high-entropy alloys. *Adv. Mater.* **30**, 1804727 (2018).

125. Su, J., Raabe, D. & Li, Z. Hierarchical microstructure design to tune the mechanical behavior of an interstitial TRIP-TWIP high-entropy alloy. *Acta Mater.* **163**, 40–54 (2019).

126. Dirras, G. et al. Elastic and plastic properties of as-cast equimolar TiHfZrTaNb high-entropy alloy. *Mater. Sci. Eng. A* **654**, 30–38 (2016).

127. Song, H., Tian, F. & Wang, D. Thermodynamic properties of refractory high entropy alloys. *J. Alloys. Compd.* **682**, 773–777 (2016).

128. Couziniė, J. P. et al. Microstructure of a near-equimolar refractory high-entropy alloy. *Mater. Lett.* **126**, 285–287 (2014).

129. Lin, C.-M., Juan, C.-C., Chang, C.-H., Tsai, C.-W. & Yeh, J.-W. Effect of Al addition on mechanical properties and microstructure of refractory AlxHfNbTaTiZr alloys. *J. Alloys. Compd.* **624**, 100–107 (2015).

130. Dirras, G. et al. Microstructural investigation of plastically deformed Ti20Zr20Hf20Nb20Ta20 high entropy alloy by X-ray diffraction and transmission electron microscopy. *Mater. Char.* **108**, 1–7 (2015).

131. Juan, C.-C. et al. Simultaneously increasing the strength and ductility of a refractory high-entropy alloy via grain refining. *Mater. Lett.* **184**, 200–203 (2016).

132. Lilensten, L. et al. Design and tensile properties of a bcc Ti-rich high-entropy alloy with transformation-induced plasticity. *Mater. Res. Lett.* **5**, 110–116 (2017).

133. Lei, Z. et al. Enhanced strength and ductility in a high-entropy alloy via ordered oxygen complexes. *Nature* **563**, 546–550 (2018).

134. Li, Z., Ludwig, A., Savan, A., Springer, H. & Raabe, D. Combinatorial metallurgical synthesis and processing of high-entropy alloys. *J. Mater. Res.* **33**, 3156–3169 (2018).

135. Holdren, J. P. *Materials Genome Initiative for Global Competitiveness* (National Science and Technology Council, Washington, 2011).

136. Kennedy, K., Stefansky, T., Dvy, G., Zackay, V. F. & Parker, E. R. Rapid method for determining ternary-alloy phase diagrams. *J. Appl. Phys.* **36**, 3808–3810 (1965).

137. Hanak, J. J. The "multiple-sample concept" in materials research: synthesis, compositional analysis, and testing of entire multicomponent systems. *J. Mater. Sci.* **5**, 964–971 (1970).

138. Xiang, X.-D. et al. A combinatorial approach to materials discovery. *Science* **268**, 1738–1740 (1995).

139. Specht, E. D. et al. Rapid structural and chemical characterization of ternary phase diagrams using synchrotron radiation. *J. Mater. Res.* **18**, 2522–2527 (2003).

140. Collins, P. C., Banerjee, R., Banerjee, S. & Fraser, H. L. Laser deposition of compositionally graded titanium-vanadium and titanium-molybdenum alloys. *Mater. Sci. Eng. A* **352**, 118–128 (2003).

141. Rar, A. et al. PVD synthesis and high-throughput property characterization of Ni-Fe-Cr alloy libraries. *Meas. Sci. Technol. A* **16**, 46–53 (2005).

142. Wilson, P., Field, R. & Kaufman, M. The use of diffusion multiples to examine the compositional dependence of phase stability and hardness of the Co−Cr−Fe−Mn−Ni high entropy alloy system. *Intermetallics* **75**, 15–24 (2016).

143. Springer, H. & Raabe, D. Rapid alloy prototyping: compositional and thermo-mechanical high throughput bulk combinatorial design of structural materials based on the example of 30Mn−1.2 C−xAl triplex steels. *Acta Mater.* **60**, 4950–4959 (2012).

144. Zhao, J.-C., Zheng, X. & Cahill, D. G. High-throughput diffusion multiples. *Mater. Today* **8**, 28–37 (2005).

145. Zhao, J.-C. Combinatorial approaches as effective tools in the study of phase diagrams and composition–structure–property relationships. *Prog. Mater. Sci.* **51**, 557–631 (2006).

146. Knoll, H. et al. Combinatorial alloy design by laser additive manufacturing. *Steel Res. Int.* **88**, 1600416 (2017).

147. Mertens, R., Sun, Z. M., Music, D. & Schneider, J. M. Effect of the composition on the structure of Cr-Al-C investigated by combinatorial thin film synthesis and ab initio calculations. *Adv. Eng. Mater.* **6**, 903–907 (2004).

148. Ludwig, A., Zarnetta, R., Hamann, S., Savan, A. & Thienhaus, S. Development of multifunctional thin films using high-throughput experimentation methods. *Int. J. Mater. Res.* **99**, 1144–1149 (2008).

149. Dobbelstein, H., Gurevich, E. L., George, E. P., Ostendorf, A. & Laplanche, G. Laser metal deposition of compositionally graded TiZrNbTa refractory high-entropy alloys using elemental powder blends. *Addit. Manuf.* **25**, 252–262 (2019).

150. Bleck, W., Raabe, D., Tasan, C. C., Springer, H. & Bausch, M. From high-entropy alloys to high-entropy steels. *J. Steel Res. Int.* **86**, 1127–1138 (2015).

151. Raabe, D. et al. Ab initio-guided design of twinning-induced plasticity steels. *MRS Bull.* **41**, 320–325 (2016).

152. Christian, J. W. & Mahajan, S. Deformation twinning. *Prog. Mater. Sci.* **39**, 1–157 (1995).

153. Steinmetz, D. R. et al. Revealing the strain-hardening behavior of twinning-induced plasticity steels: theory, simulations, experiments. *Acta Mater.* **6**, 494–510 (2013).

154. Venables, J. A. *Deformation Twinning* (Gordon & Breach, NY, 1964).

155. Friedel, J. *Dislocations* (Pergamon Press, Oxford, 1965).

156. Mahajan, S. Twin-slip and twin-twin interactions in Mo-35 at.% Re alloy. *Philos. Mag.* **23**, 781–794 (1971).

157. Mahajan, S. & Chin, G. Y. Formation of deformation twins in FCC crystals. *Acta Metall.* **21**, 1353–1363 (1973).

158. Gutierrez-Urrutia, I. & Raabe, D. Multistage strain hardening through dislocation substructure and twinning in a high strength and ductile weight-reduced Fe-Mn-Al-C steel. *Acta Mater.* **60**, 5791–5802 (2012).

159. Huang, S. et al. Temperature dependent stacking fault energy of FeCrCoNiMn high entropy alloy. *Scr. Mater.* **108**, 44–47 (2015).

160. Li, Z. & Raabe, D. Influence of compositional inhomogeneity on mechanical behavior of an interstitial dual-phase high-entropy alloy. *Mater. Chem. Phys.* **210**, 29–36 (2018).

161. Li, Z., Tasan, C. C., Pradeep, K. G. & Raabe, D. A TRIP-assisted dual-phase high-entropy alloy: grain size and phase fraction effects on deformation behavior. *Acta Mater.* **131**, 323–335 (2017).

162. Basu, S., Li, Z., Pradeep, K. G. & Raabe, D. Strain rate sensitivity of a TRIP-assisted dual-phase high-entropy alloy. *Front. Mater.* **5**, 30 (2018).

163. Nene, S. S. et al. Enhanced strength and ductility in a friction stir processing engineered dual phase high entropy alloy. *Sci. Rep.* **7**, 16167 (2017).

164. Luo, H., Li, Z. & Raabe, D. Hydrogen enhances strength and ductility of an equiatomic high-entropy alloy. *Sci. Rep.* **7**, 9892 (2017).

165. Luo, H. et al. Beating hydrogen with its own weapon: nano-twin gradients enhance embrittlement resistance of a high-entropy alloy. *Mater. Today* **21**, 1003–1009 (2018).

166. Kozelj, K. et al. Discovery of a superconducting high-entropy alloy. *Phys. Rev. Lett.* **113**, 107001 (2014).

167. Vrtnik, S. et al. Superconductivity in thermally annealed Ta-Nb-Hf-Zr-Ti high-entropy alloys. *J. Alloys. Compd.* **695**, 3530–3540 (2017).

168. Rost, C. M. et al. Entropy-stabilized oxides. *Nat. Commun.* **6**, 8485 (2015).

169. Berardan, D., Franger, S., Meena, A. K. & Dragoe, N. Room temperature lithium superionic conductivity in high entropy oxides. *J. Mater. Chem. A* **4**, 9536–9541 (2016).

170. Berardan, D., Franger, S., Dragoe, D., Meena, A. K. & Dragoe, N. Colossal dielectric constant in high entropy oxides. *Phys. Status Solidi Rapid Res. Lett.* **10**, 328–333 (2016).

171. Berardan, D., Meena, A. K., Franger, S., Herrero, C. & Dragoe, N. Controlled Jahn-Teller distortion in (MgCoNiCuZn)O-based high entropy oxides. *J. Alloys. Compd.* **704**, 693–700 (2017).

# REVIEWS

172. Sarkar, A. et al. High entropy oxides for reversible energy storage. *Nat. Commun.* **9**, 3400 (2018).
173. Anand, G., Wynn, A. P., Handley, C. M. & Freeman, C. L. Phase stability and distortion in high-entropy oxides. *Acta Mater.* **146**, 119–125 (2018).
174. Jiang, S. et al. A new class of high-entropy perovskite oxides. *Scr. Mater.* **142**, 116–120 (2018).
175. Malinovskis, P. et al. Synthesis and characterization of multicomponent (CrNbTaTiW)C films for increased hardness and corrosion resistance. *Mater. Des.* **149**, 51–62 (2018).
176. Zhou, J. et al. High-entropy carbide: a novel class of multicomponent ceramics. *Ceram. Int.* **44**, 22014–22018 (2018).
177. Dusza, J. et al. Microstructure of (Hf-Ta-Zr-Nb)C high-entropy carbide at micro and nano/atomic level. *J. Eur. Ceram. Soc.* **38**, 4303–4307 (2018).
178. Harrington, T. J. et al. Phase stability and mechanical properties of novel high entropy transition metal carbides. *Acta Mater.* **166**, 271–280 (2019).
179. Feng, L., Fahrenholtz, W. G., Hilmas, G. E. & Zhou, Y. Synthesis of single-phase high-entropy carbide powders. *Scr. Mater.* **162**, 90–93 (2019).
180. Demirskyi, D. et al. High-temperature flexural strength performance of ternary high-entropy carbide consolidated via spark plasma sintering of TaC, ZrC and NbC. *Scr. Mater.* **164**, 12–16 (2019).
181. Hsieh, T. H., Hsu, C. H., Wu, C. Y., Kao, J. Y. & Hsu, C. Y. Effects of deposition parameters on the structure and mechanical properties of high-entropy alloy nitride films. *Curr. Appl. Phys.* **18**, 512–518 (2018).
182. Mayrhofer, P. H., Kirnbauer, A., Ertelthaler, Ph. & Koller, C. M. High-entropy ceramic thin films: a case study on transition metal diborides. *Scr. Mater.* **149**, 93–97 (2018).
183. Tallarita, G., Licheri, R., Garroni, S., Orru, R. & Cao, G. Novel processing route for the fabrication of bulk high-entropy metal diborides. *Scr. Mater.* **158**, 100–104 (2019).
184. Li, Q.-L. Sheng, H. & Ma, E. Strengthening in multi-principal element alloys with local-chemical-order roughened dislocation pathways. Preprint at *arXiv* https://arxiv.org/abs/1904.07681 (2019).
185. Zhang, F. X. et al. Local structure and short-range order in a NiCoCr solid solution alloy. *Phys. Rev. Lett.* **118**, 205501 (2017).
186. Su, J., Wu, X., Raabe, D. & Li, Z. Deformation-driven bidirectional transformation promotes bulk nanostructure formation in a metastable interstitial high entropy alloy. *Acta Mater.* **167**, 23–39 (2019).
187. Wegst, U. G. K., Bai, H., Saiz, E., Tomsia, A. P. & Ritchie, R. O. Bioinspired structural materials. *Nat. Mater.* **14**, 23–36 (2015).
188. Kireeva, I. et al. Mechanisms of plastic deformation in [111]-oriented single crystals of FeNiMnCrCo high entropy alloy. *AIP Conf. Proc.* **1783**, 020090 (2016).

## Author contributions
The authors contributed equally to all aspects of the article.

## Competing interests
The authors declare no competing interests.

## Publisher's note
Springer Nature remains neutral with regard to jurisdictional claims in published maps and institutional affiliations.